International Journal of Nanomedicine

Dovepress
Taylor & Francis Group

Open Access Full Text Article

ORIGINAL RESEARCH

Magnesium Oxide Nanoparticles Loaded with 6-Gingerol: A Bioinspired Approach to Anticancer, Anti-Inflammatory, and Antioxidant Therapy

Chinnaperumal Kamaraj[1,2], Dede Heri Yuli Yanto[2], Vinoth Kumarasamy[3], Khalid A Al-Ghanim[4], Vetriselvan Subramaniyan[5], Ling Shing Wong[6], Cittrarsu Vetrivel[7]

[1]Interdisciplinary Institute of Indian System of Medicine (IIISM), Directorate of Research, SRM Institute of Science and Technology, Kattankulathur, Tamil Nadu, 603203, India; [2]Research Center for Applied Microbiology, National Research and Innovation Agency (BRIN), Cibinong Science Center, Bogor, Indonesia; [3]Department of Parasitology and Medical Entomology, Faculty of Medicine, Universiti Kebangsaan, Kuala Lumpur, Malaysia; [4]Department of Zoology, College of Science, King Saud University, Riyadh, 11451, Saudi Arabia; [5]Division of Pharmacology, School of Medical and Life Sciences, Sunway University, Selangor Darul Ehsan, 47500, Malaysia; [6]Faculty of Health and Life Sciences, INTI International University, Nilai, 71800, Malaysia; [7]International Joint Laboratory on Synthetic Biology and Biomass Biorefinery, Biofuels Institute, School of Emergency Management, School of the Environment and Safety Engineering, Jiangsu University, Zhenjiang, 212013, People's Republic of China

Correspondence: Chinnaperumal Kamaraj; Vinoth Kumarasamy, Email kamarajc@srmist.edu.in; vinoth@ukm.edu.my

Purpose: The aim of this work is to synthesize magnesium oxide nanoparticles (Gi-MgO NPs) by extracting 6-gingerol (Gi) from *Zingiber officinale* rhizomes. The Gi-MgO NPs were further investigated for anticancer, anti-inflammatory, and antioxidant activities.

Methods: The physical and chemical characteristics were examined by FT-IR, HPTLC, XRD, XPS, HR-SEM, HR-TEM, EDX, and zeta potential. Proton (^{1}H) and carbon (^{13}C) NMR spectroscopy were used to further understand the 6-gingerol compound. Gi-MgO NPs had well-dispersed spherical shapes with an average diameter of 26.18 ± 5.3 nm, a zeta potential of −16.82 ± 7.47 mV, and a polydispersity index (PDI) of 0.305, respectively. Following that, the human acute monocytic leukemia cell line (THP-1), anti-inflammatory action, and anti-oxidant properties were used to test the Gi-MgO NPs effects.

Results: The Gi-loaded nanoparticles were shown to be more effective than 6-gingerol, as evidenced by their increased toxicity against the THP-1 cell line (IC_{50} of 16.48 µg/mL) relative to control cells. Additionally, NPs demonstrated notable anti-inflammatory action with a membrane stabilization method value of 76.41% at 100 µg/mL. Subsequently, the DPPH and ABTS antioxidant properties of NPs showed significant inhibition rates of 69.82% and 78.16%, respectively.

Conclusion: The present investigation revealed Gi-MgO NPs significant anticancer effect and ability to cause apoptosis in malignant cells by modifying the expression of apoptosis-related genes; however, additional ex vivo and molecular mechanism studies are required.

Keywords: 6-gingerol, Gi-MgO NPs, NMR, HR-TEM, anticancer, THP-1 cells

Introduction

Cancer outvies the mortality factors worldwide, and in the ensuing decades, it is apprehended that the fatality rate attributable to cancer will increase dramatically.[1] Around 10 million deaths globally are attributed to cancer in 2022, and by 2040, that figure is predicted to increase to 15.3 million.[2] As a result, several cancer therapy approaches have been studied, such as radiation, surgery, and medicine. These treatments have the disadvantage of potentially damaging healthy cells.[3] Serious side effects are a major drawback for the use of drugs to treat many serious illnesses.[4] Patients typically support safe alternative therapies. Therefore, to address this expanding health issue, it is imperative to keep looking for, creating, and evaluating novel drugs with anticancer abilities. A number of traditional anticancer medications have adverse effects and exhibit drug resistance.[5] The medicine intake, metabolism, and segregation issues are only a few of the numerous causes of cancer medicine resistance. Apoptosis blockage, activating alternative pathways, modifications to target proteins and membrane lipids, and enhanced drug removal from cells are further instances of drug resistance

https://doi.org/10.2147/IJN.S531933
Received: 2 April 2025
Accepted: 26 August 2025
Published: 7 January 2026

Graphical Abstract

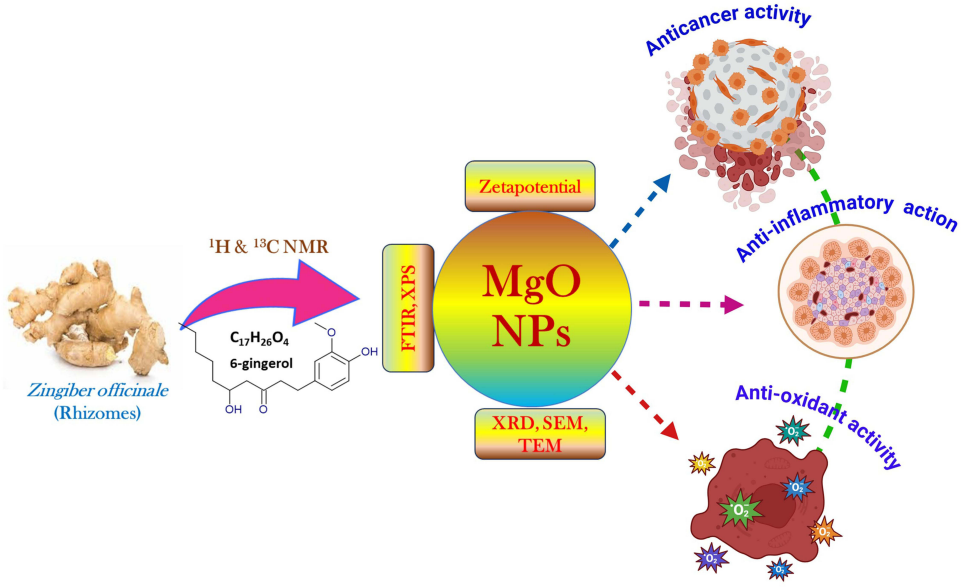

mechanisms.[6,7] Understanding natural compounds with nontoxic action mechanisms and anticancer characteristics is crucial in this context.[7,8]

Due to their significant advantages for human health and anti-cancer potentials, natural compounds and phyto-constituents are becoming more prevalent nowadays. Nedungadi et al state that ginger (*Zingiber officinale* Roscoe) rhizome has a deep-rooted importance in traditional medicine.[8] Ginger's antiseptic, antifungal, and antioxidant qualities make it a traditional plant used to cure a variety of illnesses.[9–11] As reported by Ahmed et al ginger has an effective phenolic component called gingerol, which has anti-tumor and inflammation-reducing properties.[12] The anti-cancer aspects of 6-gingerol are mainly due to its ability to affect several signalling pathways, including p53, NF-kB, AKT, ERK1/2, and JNK.[13–15] Despite its potential, there are several challenges associated with 6-gingerol that limit its broader applications, such as low water solubility and sensitivity to temperature, pH, and oxygen.[16,17] Therefore, fabrication of nano drug delivery avenues is indispensable for ensuring the efficient and precise delivery.

Recently, a substantial focus on cancer research in developing a nanotechnology-based delivery system for its medications has attained the spotlight. Due to a decrease in toxicity, the introduction of nanocarriers into drug delivery systems has greatly enhanced the solubility, stability, and chemotherapeutic effects of drugs. [17–19] Metal oxides, a broad class of nanomaterials that include magnetic and nano-electronic nanocarriers, transpired extensively in medical applications like drug delivery. [20–25] Magnesium oxide (MgO) are promising option for bio-imaging and drug administration because of its superior biocompatibility, non-toxicity, remarkable stability, and targeted selectivity.[26,27] Furthermore, MgO nanoparticles anti-microbial and anti-inflammatory abilities expand their biological applicability in relation to skin inflammation.[28–31] Additionally, as stated by Anicic et al magnesium oxide is considered safe for human intake by the FDA.[32] MgO nanoparticles have a number of advantageous characteristics, such as increased surface, enhanced charge, and exclusive crystal arrangements, which allow for easy interaction with a number of biological processes.[33,34] Biological tagging, wound treatment, blood sampling, drug delivery through encapsulation, relief from stomach issues and heartburn, and promoting bone healing are just a few of the uses for magnesium oxide nanoparticles.[35–37] Furthermore, MgO nanoparticles have demonstrated potential as antibacterial, antifungal[35,36,38,39,] anticancer,[41] antioxidant, and antidiabetic agents.[42] Moreover, MgO nanoparticles have been applied in tissue engineering,[43,44] bioimaging,[44] and drug delivery.[45] Because of its growing use in biomedicine, it is crucial to investigate novel biosynthetic techniques for the manufacture of MgO NPs. The fundamental intent of this research is to employ the phenolic compound 6-gingerol-loaded magnesium oxide nanoparticles to make potential anticancer, antioxidant,

and anti-inflammatory applications and characterize the NPs through HPTLC, proton (^{1}H) and carbon (^{13}C) NMR, FTIR, XPS, XRD, HR-SEM, Zeta potential, and HR-TEM study; determine the physicochemical properties; and then employ 6-gingerol employ the in silico molecular docking and molecular dynamic simulations of the Sirt2 protein receptor. To the benefit of the biomedical and pharmaceutical sectors, the use of nanoparticles can offer a sustainable and environmentally friendly alternative for traditional anti-inflammatory and anticancer drugs.

Materials and Methods

Chemicals and Reagents

All chemicals, gingerol standards, and kits for the anti-inflammatory, anticancer, and antioxidant assays were supplied by Sigma Aldrich (Bangalore, India). Sigma Aldrich supplied $Mg(NO_3)_2 \cdot 6H_2O$ for nanoparticle production, along with reference standards including vitamin C (≥99%), acetylsalicylic acid (aspirin), MTT (3-(4,5-dimethylthiazol-2-yl)-2,5-diphenyltetrazolium bromide), Adriamycin (≥95%), and 10% phosphate-buffered saline (PBS). The following materials—sodium hydroxide, 2,2′-azino-bis (3-ethyl benzothiazoline-6-sulfonic acid) (ABTS), and 2,2-diphenyl-1-picrylhydrazyl (DPPH)—were bought from Hi-Media in Mumbai, India. Acridine orange/propidium iodide (AO/PI) dye, Tween-20, ethanol, chloroform, and dimethyl sulfoxide (DMSO) were all supplied by SRL. The entire experiment was conducted using deionized (D_2H_2O), double-distilled water. The glassware was untainted with diluted nitric acid and rinsed comprehensively with distilled water to remove residues, then dried in a glass dryer to eliminate moisture.

Extraction of [6]-Gingerol

The extraction method of Singh et al[46] was adopted to extract 6-gingerol from freshly dried rhizomes of *Z. officinale* (Zingiberaceae) that were bought from the Potheri vegetable market. The obtained ginger (4 kg) was cleaned with tap water to remove unwanted debris, then the ginger was sliced into small pieces and dried in a shaded environment for 14 days. The dried sample (1.85 kg) was ground using an electrical stainless-steel blender, and powder was extracted with chloroform at room temperature (26±2.00°C). The crude extract (116.78 g) was obtained by filtering and concentrating the extraction under vacuum conditions using a rotary evaporator. To get a high yield of the fraction in 6-gingerol, the crude extract was processed to column chromatography using a hexane-ethyl acetate (9:1) combination over silica gel (230–400 µm mesh). Functional groups were identified through FT-IR, and structural characterization was done by carbon (^{13}C) and proton (^{1}H) NMR.

High-Performance Thin-Layer Chromatography (HPTLC)

The mobile phase used for the HPTLC analysis of compound purity consisted of methanol, water, ethyl acetate, and chloroform in a volume ratio of 20:2.5:0.5:2 (v/v). The analysis was developed on a Silica Gel 60 F254 HPTLC plate (20 × 10 cm, Merck, Germany, #5642). Standard solutions of gingerol (5.0 µL with each concentration of 1 mg/mL) were applied in bands measuring 10 mm. The application of samples was carried out using a 100 µL syringe fitted with a CAMAG Linomat IV automated spray-on band applicator. The applicator was configured as follows: a 4 mm distance, 1.5 cm from the plate's side edge, 2 cm from the plate's bottom, a 10 mm band length, and an application rate of 10 sec/µL.

Densitometric analysis of the spectra was performed using the WINCATS software (Version 4.X) and the CAMAG TLC Scanner 3. The operational parameters were set as follows: a scanning rate of 20 mm/s, a 5×0.1-mm slit, and a monochromator bandwidth of 20 nm, with scans conducted at ideal wavelengths of 254 nm, 366 nm, and in the visible range. The measurements were recorded in both absorption and reflection modes, as per the methodology outlined by Wagner and Bladt,[47] and Maleš et al.[48]

NMR Analysis of 6-Gingerol

The ^{1}H NMR (proton nuclear magnetic resonance) spectrum was utilized to analyze the isolated 6-gingerol using a Bruker BBFO system operating at 500 MHz. In contrast, Bruker Advance III equipment operating at 100.64 MHz was used to record the carbon nuclear magnetic resonance (^{13}C NMR) spectra. The solvent utilized in the analysis of the NMR spectra was $CDCl_3$. Relative to tetramethylsilane (TMS, $\delta = 0$ ppm), the ^{1}H NMR chemical shift was calibrated

using deuterated chloroform ($CDCl_3$, δ = 7.26 ppm singlet) as the reference. The reference ^{13}C NMR spectra were calculated with the following formula: $CDCl_3$, δ = 77.5 ppm.

Drug Loading and Magnesium Nano-Synthesis

In general, a synthesis involves 50 mL of D_2H_2O, 10 mg of isolated 6-gingerol, and 1 mL of Tween 20 in a flask. The mixture is heated to 40°C for effective abstraction (15 min), cooled to ambient temperature, and then ultrasonicated for 1 h. After 1h the same process was taken; at the time, 4 mL of Tween 20 was added and then sonicated. At 5h the final solution was turned completely milky white. After allowing the reaction mixture to cool to 30°C, the reaction component was gradually filled with (0.5 M) $Mg(NO_3)_2{\cdot}6H_2O$. Four hours were given to the reaction, which was agitated at 300 rpm. The resulting white precipitates were passed through a filter and dried in the oven for two hours to obtain the 6-gingerol (Gi)-loaded magnesium NPs. According to the research by Kazazi et al,[17] the generated nanoparticles were stored in a sealed sample container. The concoction method was optimized to produce better results. The ratio of precursor salt to Gi dosage was changed from 20:10 to 20:20 in order to interrogate the effect of compound dosage on the conception of magnesium nanoparticles. At the same time, other reaction parameters like pH (4.2 at 25°C), temperature (40 ± 2°C), and precursor salt concentration (0.1 M) remained constant. Similarly, to optimize the synthesis methodology, the effects of temperature (60, 50, 40, and 30°C), pH (3.2, 4.2, 7.2, and 9.2 at 25°C), and concentration of precursor solution (2, 1, 0.5, and 0.1 M) on the values of Mg NPs were also investigated.

Fourier Transforms Infrared Spectroscopy (FT-IR)

The chemical moieties confined to 6-gingerol and Gi-Mg NPs were analyzed using FT-IR with a Shimadzu Model 8300 (Shimadzu Corporation, Tokyo, Japan).[49] In brief, KBr (potassium bromide pellets) was used to make a sample of magnesium nanoparticles loaded with Gi and 6-gingerol at a ratio of 1:99. Using the air as a background, the spectra obtained in this manner were analyzed in the 4000–400 cm^{-1} mid-infrared range using Spectrum 10 software.

X-Ray Diffraction Analysis of Gi-Mg NPs

The crystalline nature and structural properties of biogenic Gi-Mg NPs were examined using the XRD {BRUKER D8 Advance (Davinci) system from the USA} fitted with a CuKα radiation, λ = 1.5406 A°. The analysis was conducted at 10 mA and 30 kV, with a scanning speed of 2°/min, the diffraction intensity was recorded, and the measured values of 2θ varied from 0° to 80°.

Sample Preparation for Microscopy Analysis

For HR-SEM imaging, the dried powder of Gi-Mg NPs was carefully placed on carbon-coated aluminum stubs and then sputter-coated with a small layer of gold to improve conductivity and resolution. For HR-TEM investigation, a freshly produced aqueous suspension of Gi-Mg NPs was ultrasonically dispersed for 10 m. A 10 µL suspension was drop-cast onto carbon-coated copper grids, excess was removed with filter paper, and air-dried at room temperature for imaging and SAED analysis. Elemental composition was determined using EDX together with HR-SEM, using the identical gold-coated samples used for SEM analysis. For dynamic light scattering (DLS) and zeta potential measurement, Gi-Mg NPs were suspended in deionized water, ultrasonicated for 10 minutes to ensure adequate dispersion, and then examined at room temperature. These various preparation methods were implemented to ensure the ideal conditions required for each analytical technique.

Microscopy Analysis of Gi-Mg NPs

Gi-MgO NPs were examined to find out their structure, morphology, and particle size using High-Resolution Scanning Electron Microscopy (HR-SEM, Thermo Scientific Apreo S) for surface features and High-Resolution Transmission Electron Microscopy (HR-TEM, JEOL JEM-2100 Plus) for internal structure and size characterization. Additionally, EDX analysis of Gi-MgO NPs samples was combined with HR-TEM and utilized to determine the NPs elemental composition. Furthermore, the selected area electron diffraction (SAED) and mapping analyses were conducted using HR-TEM. The Gi-MgO NPs suspension was first immersed in an ultrasonic bath for 10min to prepare for the analysis. In

a carbon-coated copper grid, 10 µL of the sample was exposed for approximately 30 seconds. After using filter paper to remove any extra samples, the grids were allowed to dry. Dynamic light scattering (DLS) was used to investigate the zeta potential and particle size distribution of bio-encapsulated Gi-Mg NPs using a Malvern Zetasizer Nano range equipment (Malvern Instruments Ltd., Malvern, UK).

X-Ray Photoelectron Spectroscopy (XPS)

The surface elemental composition of the bioencapsulated Gi-MgO NPs was examined using a Thermo Scientific K-ALPHA (K-Alpha photoelectron spectrometer, Thermo Fisher Scientific Inc., USA) in combination with a monochromatic X-ray ALK-alpha radiation (− 10 to 1350 eV) source of ionizing radiation. The analysis was performed with the contingents: The spot's dimensions were reported by Hamza et al[50] to be 500 µm. A pressure adjustment of 10–8 mbar was used to create the samples. Mg3d5/2 (ΔBE: 0.45 eV) and C 1s (ΔBE: 0.82 eV) signals were used to calibrate the energy. The energy of the full and narrow spectrum passes was 20 and 50 eV, respectively.

The elemental configuration on the surface of bioencapsulated Gi-MgO NPs was examined using XPS with a Thermo Scientific K-Alpha photoelectron spectrometer (Thermo Fisher Scientific Inc., USA) and Al Kα radiation (1486.6 eV). The evaluation was conducted under a pressure of 10^8 mbar, with a spot size of 500 µm. Calibration was done using the Mg 3d5/2 (ΔBE: 0.45 eV) and C 1s (ΔBE: 0.82 eV) reference signals. Full-spectrum and narrow-scan pass energies were set to 20 eV and 50 eV, respectively.

THP-1 Cell Cultures and Exposure to Gi-Mg NPs

The THP-1 human monocytic leukemia cell line (RRID: CVCL0006) was obtained from NCCS, Pune, India, and cultured at a density of 1.25×10^5 cells/cm^2 in 24-well plates. The culture medium consisted of RPMI-1640 supplemented with 10% FBS, 100 IU/mL of penicillin, 100 µg/mL of streptomycin, 2.5 µg/mL of amphotericin B, 0.05 mM 2-mercaptoethanol, and 100 ng/mL of phorbol 12-myristate 13-acetate to promote macrophage differentiation. The cells were incubated at 37°C with 5% CO_2 for 48 h. After medium replacement and reaching 70–80% confluency, cells were seeded at 5×10^4 cells/mL in a 96-well plate and incubated for 48 h. Cytotoxicity was assessed by treating the cells with Gi and Gi-MgO NPs (6.25–100 µg/mL, final DMSO concentration 0.025%) for 48 h. Afterward, 100 µL of MTT (0.5 mg/mL) solution was added, and after 4 h at 37°C, crystals were dissolved in isopropyl alcohol. Absorbance at 595 nm was measured using a Thermo Multiskan 96-well reader. Doxorubicin (100 µM) was used as a positive control.[51,52]

Flow Cytometer Assay

Apoptosis was assessed using the FITC Annexin V/Dead Cell Apoptosis Kit with flow cytometry analysis conducted on a BD FACS Calibur (BD, USA), following the provided guidelines to measure the amount of apoptosis caused by Gi and Gi-MgO NPs. THP-1 cells (1×10^5 cells/mL) were cultured in 6-well plates (Corning) and incubated with 5% CO_2 for 24 hours. Once the cells reached 80% confluence, fresh media containing NPs at the IC50 concentration was introduced. Following 24 hours of incubation, cells were rinsed with PBS and prepared for flow cytometry analysis. The LSM-700 confocal laser scanning microscope (Carl Zeiss in Germany) was used for the imaging investigations. After that, these cells were treated with PBS that included 50 µL of ethidium bromide (EB) and acridine orange (AO). At emission wavelengths of 520 and 650 nm, respectively, the labelled cells were seen using CLSM to image the populations of living (green fluorescence) and dead (red fluorescence) cells.

Cell Cycle Assay

The cell cycle's sub-G1 phase was evaluated using a commercially available cell cycle analysis kit. In summary, THP-1 cells were maintained at a concentration of 1×10^5 cells/mL. After a 24-hour treatment with 6-gingerol and Gi-MgO NPs at their respective IC_{50} concentrations of 29.12 µg/mL and 16.48 µg/mL, the cells were centrifuged and preserved. They were then reconstituted in a solution infused with RNase A and propidium iodide (PI), followed by PBS washing. The FL2 channel was utilized to identify sub-G1 peaks on a flow cytometer.

Antioxidant Activity Studies

To test Gi-MgO NPs ability to suppress DPPH and ABTS free radicals, different doses (20–100 µg/mL) were produced. Then each microtube was filled with a pre-measured quantity of free radicals. The samples were tested for absorbance at 593 nm after 15 min of incubation. For the formation of the standard curve at 593 nm, ascorbic acid was utilized at assorted concentrations (20–100 µg/mL). Using the following formula (**1**), where percentages are replaced with integers to get the inhibition percentage:

$$\%\ \text{Free radicals scavenging} = {}_{\text{OD}}\,\text{Control} - {}_{\text{OD}}\,\text{Sample} \;/\; {}_{\text{OD}}\,\text{Control} \times 100 \tag{1}$$

Anti-Inflammatory Activity

Inhibition of Protein Denaturation

The effectiveness of Gi-MgO NPs in lowering inflammation was evaluated using the protein denaturation inhibition assay. A 0.45 mL aliquot of a 5% BSA solution was incorporated into a reaction mixture (0.5 mL, pH 6.3), and 1 N HCl was used to amend the pH. After adding NPs (12.5–200 µg/mL), the mixture was allowed to be incubated for 20 minutes at 37°C and then boiled for 5 minutes at 57°C. At 600 nm, the turbidity was measured upon chilling with 2.5 mL PBS. Using the proper formula, the % inhibition of protein denaturation was computed (2):

$$\text{Inhibition}\ (\%) = \left(\text{Abs}_{\,\text{Control}} - \text{Abs}_{\,\text{sample}}\right) / \text{Abs}_{\,\text{control}} \times 100 \tag{2}$$

Membrane Stabilization Assay

Lysosomal enzymes, which develop during inflammation, are linked to various diseases and may impact membrane function in both acute and chronic inflammation. Human red blood cells (HRBCs) were incubated with varying concentrations of Gi-MgO NPs (12.5–200 µg/mL), with aspirin as the reference standard and a blank containing no NPs or standard. The mixture was combined with 0.5 mL H/RBC solution, 2 mL hyposaline, and 1 mL PBS, then placed at 37°C for 30 minutes of incubation. After centrifugation at 3000 rpm for 15 minutes, hemoglobin concentration was measured at 550 nm using spectrophotometry. The percentage of hemolysis was calculated assuming the control group exhibited 100% hemolysis, and the formula was applied to determine the protection and hemolysis ratios (3):

$$\text{Inhibition}\ (\%) = \left(\text{Abs}_{\,\text{Control}} - \text{Abs}_{\,\text{Sample}}\right) / \text{Abs}_{\,\text{control}} \times 100 \tag{3}$$

Molecular Docking Study

The RCSB-PDB database provided us with a high-resolution image of the target protein. The human Sirt2 protein's crystal structure (PDB ID 4RMG) was estimated using the 1.88 Å resolution X-ray diffraction technique. Using Molegro Molecular Viewer (MMV) to extract the co-crystallized ligand and water molecules, we synthesized the resulting protein and stored it in PDB format. In mol format, we sketched the ligands' three-dimensional configuration. Utilizing the protein data bank (PDB file) format, the Chem3D Pro 12.0 program reduced the energy of the ligand compound sketches. The active binding site of the drug target protein was predicted using the Supercomputing Facility for Bioinformatics and Computational Biology at IIT Delhi. Molecular docking was employed to assess the binding affinity of 6-gingerol with the Sirt2 protein. The docking process included grid creation, ligand and protein preparation, and ligand docking. AutoDock Vina was used for the molecular docking of the ligand with the target protein. We used Biovia Discovery Studio Visualizer 2021 to analyze and visualize the protein-ligand complex binding interaction.

Molecular Dynamics Simulation Study

Molecular dynamics (MD) simulation is a key strategy for understanding the structure and function of biological target proteins. It provides insights into the dynamics and biomolecular activities of the target. MD simulation of the Sirt2 protein and gingerol complex was performed using Desmond. Protein preparation included adding hydrogens, completing missing amino acid side chains, optimizing loops, assigning H-bonds, and adjusting water orientations at pH 7.0. The system was constructed utilizing the TIP3P solvent model and filled with water molecules, defined by an orthorhombic box (10 Å × 10 Å × 10 Å). Sodium ions were added for electrical neutrality. The simulation ran for 100 ns at 300 K and

1.01 bar at a constant volume and utilized the Smooth Particle Mesh Ewald (PME) method in the NPT ensemble. The results, including ligand-protein interactions, root-mean-square deviation (RMSD), and fluctuation (RMSF), were analyzed using the Simulation Interaction Diagram wizard.

Statistical Analysis

GraphPad Prism Version 8 (GraphPad Software, Inc., San Diego, CA, USA) was used to accomplish all of the outcomes that were acquired. The significance of the differences between statistical groups was evaluated using a one-way ANOVA. The significant difference between the treatment and control groups was found to be $P < 0.05$. All assessments were pulled off in three repeats.

Results and Discussion

Validation of 6-Gingerol by HPTLC Method

A precise and efficient densitometric HPTLC method for analyzing 6-gingerol was developed by optimizing the mobile phase composition. The ethyl acetate: n-hexane (30:70, v/v) mobile phase resulted in a well-resolved, symmetrical peak with an Rf value of 0.73 (Figure 1A–C). A maximum of 10 min is required for chamber saturation. As a result, 530 nm was determined as the wavelength for UV densitometry based on the bands' UV spectra, which revealed maximal absorption at that wavelength (Figure 1A–C). Foudah et al[53] reported that a 6.5:3.5 (% (v/v) ethanol-water mixture produced compact, symmetric, and well-resolved densitometric peaks of 6-gingerol with an Rf of 0.53 ± 0.01. Similarly, Khan et al[54] achieved comparable results using a 7:2:1 (v/v/v) acetonitrile-water-formic acid mixture at 25 ± 2°C, with plates scanned at 500 nm. Compact spots with R_f values of 0.73±0.04 were seen for 6-gingerol in the system. According to the study's findings, a variety of plant extracts and commercial formulations could successfully employ the suggested analytical technique to simultaneously quantify 6-gingerol.

NMR Spectral Characterizations

The isolated 6-gingerol was characterized by the nature of the solid (pale yellow), melting point (31.7 °C), R_f (ethyl acetate: *n*-hexane 3:7) 0.73 ±0.01, FT-IR (KBr) (cm^{-1}), ^{1}H NMR ($CDCl_3$, 500 MHz): δH, and ^{13}C NMR (125 MHz, in $CDCl_3$): δC (Figure 2A–C). IR (KBr) (cm^{-1}) revealed the different functional groups, such as 3434 (O-H), 2930 (C-H), 2859 (C-H), 1704 (C=O), 1289 (C-O), and 1136 (C-O-C). ^{1}H NMR ($CDCl_3$, 500 MHz): δH 7.28 (s, Aro-OH), 6.63–6.82 (m, Aro-H), 5.91 (s, Ali-OH), 4.02–4.05 (s, 6H), 3.84 (s, Aro-OCH_3), 2.81–2.85 (t, (-CH_2) −3H), 2.71–2.58 (t, (-CH_2) −3H), 0.87–0.90 (t, (-CH_3)-4H). ^{13}C NMR (125 MHz, in $CDCl_3$): δC 211.63, 146.72, 132.75, 120.84, 114.68, 111.27, 77.52, 77.27, 77.01, 67.84, 55.99, 49.49, 45.53, 36.59, 31.84, 29.66, 29.37, 25.58, 25.25, 23.70, 14.14). The obtained data were compared with the previous literature.[55,56]

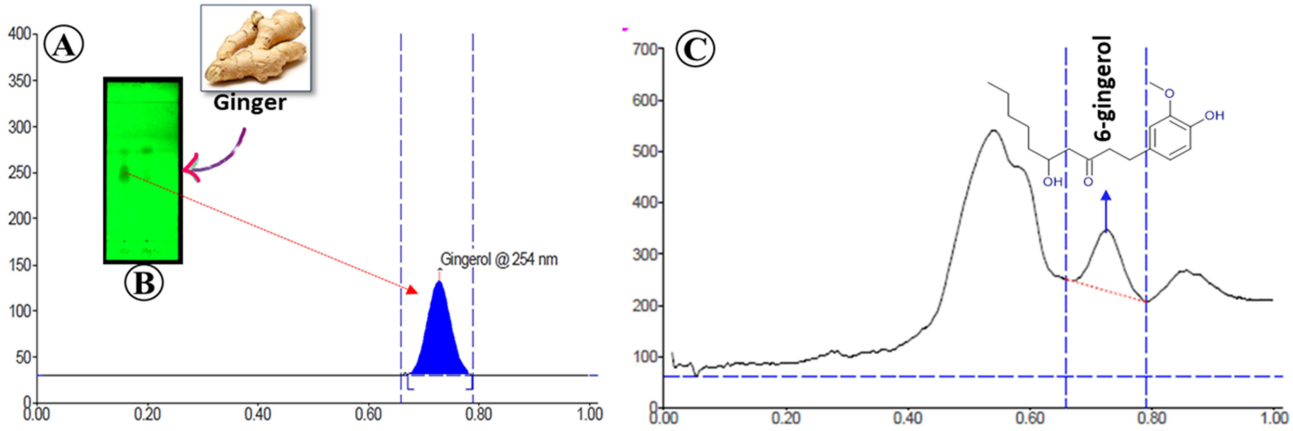

Figure 1 HPTLC fingerprint of 6-gingerol and standard densitogram (**A**) gingerol standard (**B**) TLC fingerprint and (**C**) 6-gingerol loaded Mg NPs at R_f 0.73 ±0.01.

https://doi.org/10.2147/IJN.S531933

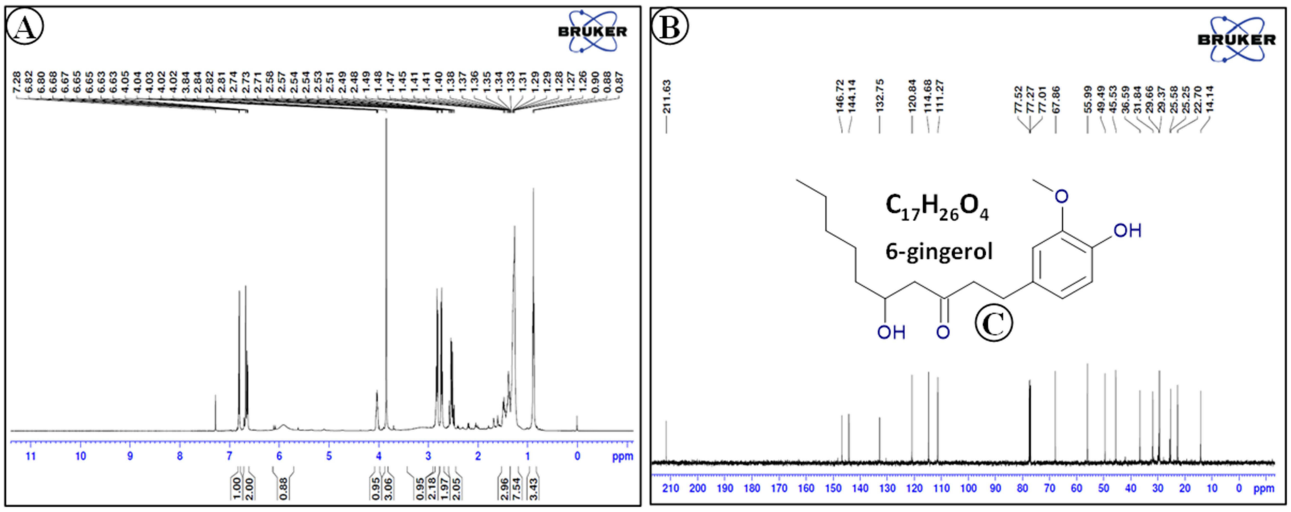

Figure 2 NMR characterization of (**A**) ^{1}H NMR spectrum, (**B**) ^{13}C NMR spectrum, and (**C**) structure of 6-gingerol.

Spectral Analysis for Functional Moieties

The results of the FT-IR study, which recorded a wavenumber between 4000 and 400 cm^{-1}.. As shown in Figure 3A, identifying the 6-gingerol that reduces metal precursors to produce Gi-MgO NPs. The peak observed by 6-gingerol at 3434.10, 2930.31, 2859.41, 1704.63, 1606.71, 1517.23, 1452.45, 1378.96, 1269.65, 1136.18, 1035.29, 809.29, 728.05, 625.70, and 557.74 cm^{-1}. Gi-Mg NPs revealed 3830.98, 3439.04, 2932.63, 2406.85, 2353.59, 2081.28, 1641.45, 1518.24, 1384.80, 1142.91, 1020.63, 951.92, 824.33, 713.11, and 670.68 cm^{-1}, respectively. The –OH stretching band is shown by the peak seen at 3830 cm^{-1}..[57]

According to Dobrucka,[58] a peak at 3439 cm^{-1} typifies O–H stretching vibration (hydroxyl groups), overlapping with NH stretching of amines. FT-IR analysis revealed a peak at 1641 cm^{-1}, indicating primary amine (N–H) bending, possibly overlapping with amide or carboxylate salt. The peak at 1518 cm^{-1} is associated with the C=O stretching of carboxylate salt and CO_3^{2-}/CO_2 adsorption on MgO-NPs surfaces.[50,59] In catalytic processes, these functional groups on magnesium nanoparticles are important.[60] The peak at 1020 cm^{-1} corresponds to C–H out-of-plane bend and Mg–OH stretching,[61] while the 951 cm^{-1} peak represents C–O stretching, trans-C–H bend, and P–O for molecules containing phosphate.[62] Based on the

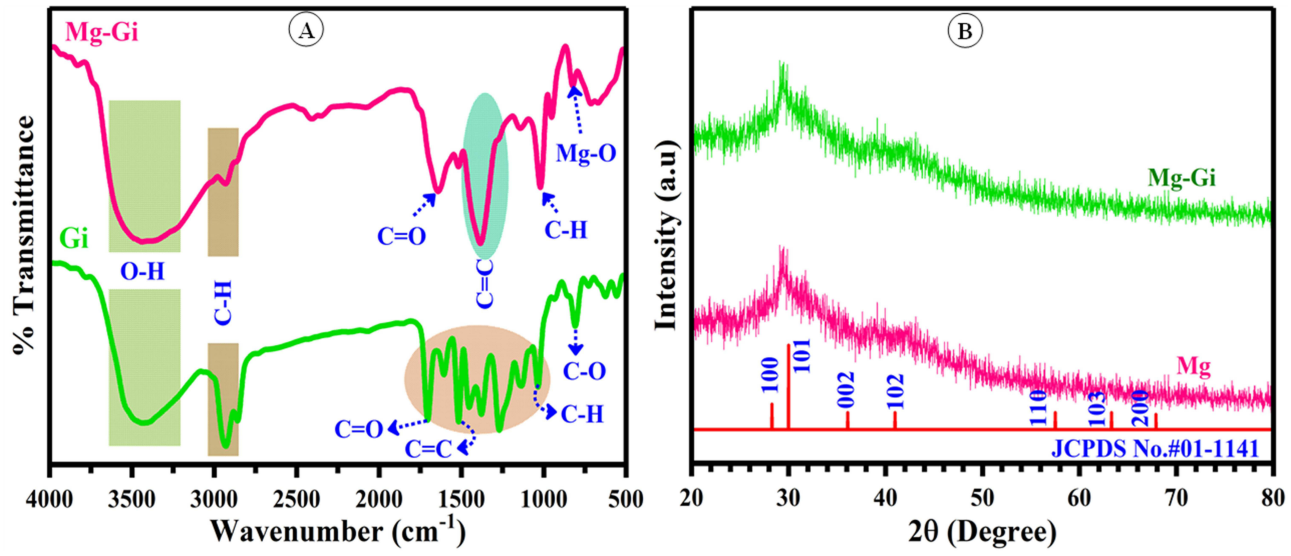

Figure 3 6-gingerol and Gi loaded MgO NPs (**A**)FT-IR spectrum, and (**B**) XRD pattern of Gi-Mg NPs.

https://doi.org/10.2147/IJN.S531933

previous research,[57,63,64] the FT-IR peaks detected at a wavenumber between 400 and 700 cm^{-1} validated the successful production of Mg NPs. The peaks seen in FT-IR spectra correspond to the 6-gingerol, which acts to stabilize and reduce magnesium nanoparticles.

XRD Analysis

XRD analysis of Gi-MgO NPs revealed characteristic diffraction peaks at 2θ values of 28.2°, 32.6°, 36.4°, 42.2°, 56.5°, 62.4°, and 68.3°, corresponding to the (100), (101), (002), (102), (110), (103), and (200) planes of crystalline MgO NPs (JCPDS file No. 01–1141). The relatively broad nature of the peaks confirms the nanoscale crystallinity of the synthesized material (Figure 3B). According to the findings, Rhizopus oryzae-formed MgO-NPs had crystallographic structures that matched the JCPDS standard (JCPDS file No. 01–1141).[65] XPS examination confirms that oxide, specifically magnesium $(OH)_2$ and magnesium oxide, is present in the sample based on the detected XRD peaks.

Lekota et al[66] identified distinct diffraction peaks at 2θ° values of 36.4° (102) and 62.4° (200), pertaining to the presence of $Mg(OH)_2$. Furthermore, they observed peaks at 42.2° (110) and 62.4° (200), indicating the presence of cubic MgO-NPs. Similarly, Hassan et al[67] reported the myco-synthesized MgO-NPs were crystalline in nature, showing five prominent peaks at 36.9°, 42.6°, 62.2°, 75.4°, and 78.6°, which were assigned to the (111), (200), (220), (311), and (222) planes, respectively. The formation of crystalline MgO-NPs was corroborated by the above-mentioned findings.

In the case of the current study, the XRD pattern of Gi-MgO NPs revealed a well-defined crystalline structure. The crystal size was calculated to be 50 nm using the Debye-Scherrer equation, which is commonly used for determining the size of nanoparticles from X-ray diffraction data. This supports the presence of crystalline MgO-NPs and suggests that Gi-Mg NPs have a relatively small and uniform particle size.

SEM, EDX, and TEM Analysis

The surface configuration, aggregates, and qualitative and quantitative chemical constituents of Gi-MgO NPs were determined through the application of SEM-EDX analysis. The SEM photographs of Gi-MgO NPs showed a perfectly

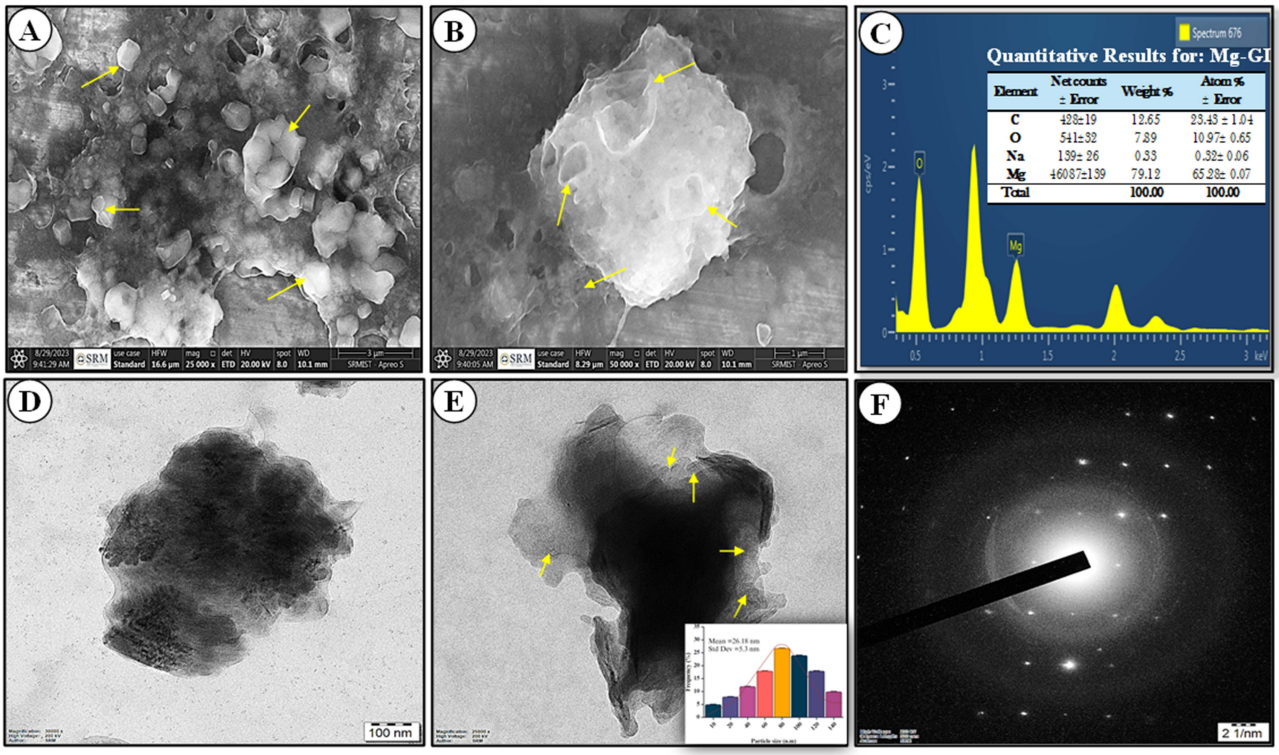

Figure 4 6-gingerol loaded MgO NPs. (**A** and **B**) HR-SEM images at different magnifications, with yellow arrows highlighting the porous spherical morphology of Gi-MgO NPs, (**C**). EDX of Gi-Mg NPs, (**D** and **E**) HR-TEM micrographs (scale bar at 50 nm), and (**F**) selected area electron diffraction (SAED) pattern of Gi- Mg NPs.

https://doi.org/10.2147/IJN.S531933

porous nature, evenly distributed, spherical, and not aggregated (Figure 4A and B). Mg and O are present in the EDX profile as well, with weights of 79.12 and 7.89% and atomic percentages of 65.28 and 10.97%; in additional peaks, there were 12.65% and 0.33% for C and Na, respectively (Figure 4C). Our analysis supports Dobrucka's[58] observations that peaks in the energy range of 0.5 to 1.5 keV are suggestive of a successful synthesis of MgO-NPs. Elements including Mg, O, Al, Si, K, and Ca are present in the EDX profile of MgO-NPs made with water extract from *Artemisia abrotanum*, with corresponding weight percentages of 13.9%, 39.4%, 1.4%, 0.3%, 0.8%, and 0.5%, respectively. According to Alsharif et al,[68] the study revealed that the presence of capping and stabilizing substances, such as proteins, enzymes, polysaccharides, and amino acids, which may hydrolyze and interact with the X-ray during analysis, is responsible for the identification of elements other than Mg and O.

TEM images (Figure 4D and E) show that 6-gingerol successfully reduces, caps, and stabilizes spherical MgO-NPs with an average size of 26.18 ± 5.3 nm, ranging from 12.5 to 57.6 nm. Similar results were seen with *Aspergillus carbonarious* D-1 metabolites, which produced spherical MgO-NPs ranging from 20 to 80 nm,[64] and *Carica papaya* leaf extract, which synthesized MgO-NPs averaging 100 nm in size.[20] The aforementioned findings underscore the effectiveness of 6-gingerol in controlling nanoparticle size and morphology. These outcomes illustrate that using the secondary metabolites of discovered 6-gingerol, Gi-Mg NPs with small sizes might be synthesized in a greener way. The activity of nanoparticles (NPs) is closely linked to their size and shape, with smaller particles exhibiting greater activity.[69,70] For example, MgO-NPs with sizes of 35.9 nm, 47.3 nm, and larger micron-sized particles (2145.9 nm) demonstrated varying bactericidal effectiveness against *Bacillus subtilis*. The bactericidal rates were 96.12%, 94.46%, and 75.71%, respectively.[71] The metabolites of various organisms (bacteria, actinomycetes, algae, fungi, and plants), as well as between different species within the same genus, may be responsible for the variations in sizes and shapes of nanoparticles (NPs) produced using environmentally friendly methods. The powder's high crystallinity results in well-defined Debye-Scherrer diffraction rings in the SAED pattern, as shown in Figure 4F. These rings are associated with the wurtzite hexagonal structure's reflections (100), (101), (002), (102), (110), (103), and (200). The SAED pattern shows no extra rings resulting from any crystalline defects.

Particle Size and Zeta Potential

Formulated Gi-loaded MgO NPs were characterized for zeta potential and average particle size (Figure 5A and B). The Gi-MgO NPs exhibited a small particle size of 92 nm, suggesting latent advantages for drug delivery and catalysis. These nanoparticles are stable, with a zeta potential of −16.82 ± 7.47 mV, indicating strong electrostatic repulsion that prevents aggregation. A Polydispersity Index (PDI) of 0.305 indicates a considerable degree of particle size distribution, implying that the nanoparticles are not completely uniform in size. These results align with previous studies by Raliya and Tarafdar,[72] Ammulu et al,[73] and Sami,[74] respectively.

X-Ray Photoelectron Spectroscopy (XPS) Analysis

Figure 6A displays the XPS survey spectra of Gi-MgO NPs loaded with 6-gingerol. A number of peaks of Mg (O1s, Mg2s, C1s, Mg2p, and Mg2s) were used to characterize at different binding energies; further related ions included O (1s, 2s, Mg KLL, and OKLL) and Cl (2p and 1s). Characteristic peaks at 280.00 eV (O-C-O), 285.36 eV (C=C), and 286.38 eV (C-C), along with additional peaks at 284.2 eV (C (C, N, H)) and 285.65 eV (C-O-C), were displayed by high-resolution XPS spectra of nano-MgO (Figure 6A).[75–78] The Mg 2s spectra (Figure 6B) show peaks at 88.67 eV, 89.74 eV, and 91.65 eV, which correspond to MgO (82.64%) and $Mg(OH)_2$ (15.14%). FT-IR analysis indicates that the polysaccharide structure includes amide and carbonyl groups. The C1s peak (Figure 6C) reflects carbon from air exposure. The O 1s spectra (Figure 5d) reveal carboxyl groups, with peaks at 532.24 eV (C-OH) and 530.16 eV (C=O).[50,79] These results suggest that nano-MgO primarily consists of MgO with hydroxyl and carboxyl groups on its surface.

6-Gingerol and Gi-Mg NPs Inhibition of THP-1 Cell Growth

The MTT test was utilized to examine the cytotoxic impact of 6-gingerol-loaded magnesium nanoparticles on THP-1 cells. In our investigation, THP-1 cell viability at varying concentrations of Gi-MgO NPs showed greater impacts on THP-1 cells than did the 6-gingerol molecule. Cell viability reduced when the quantity of Gi-MgO NPs rose, as seen in

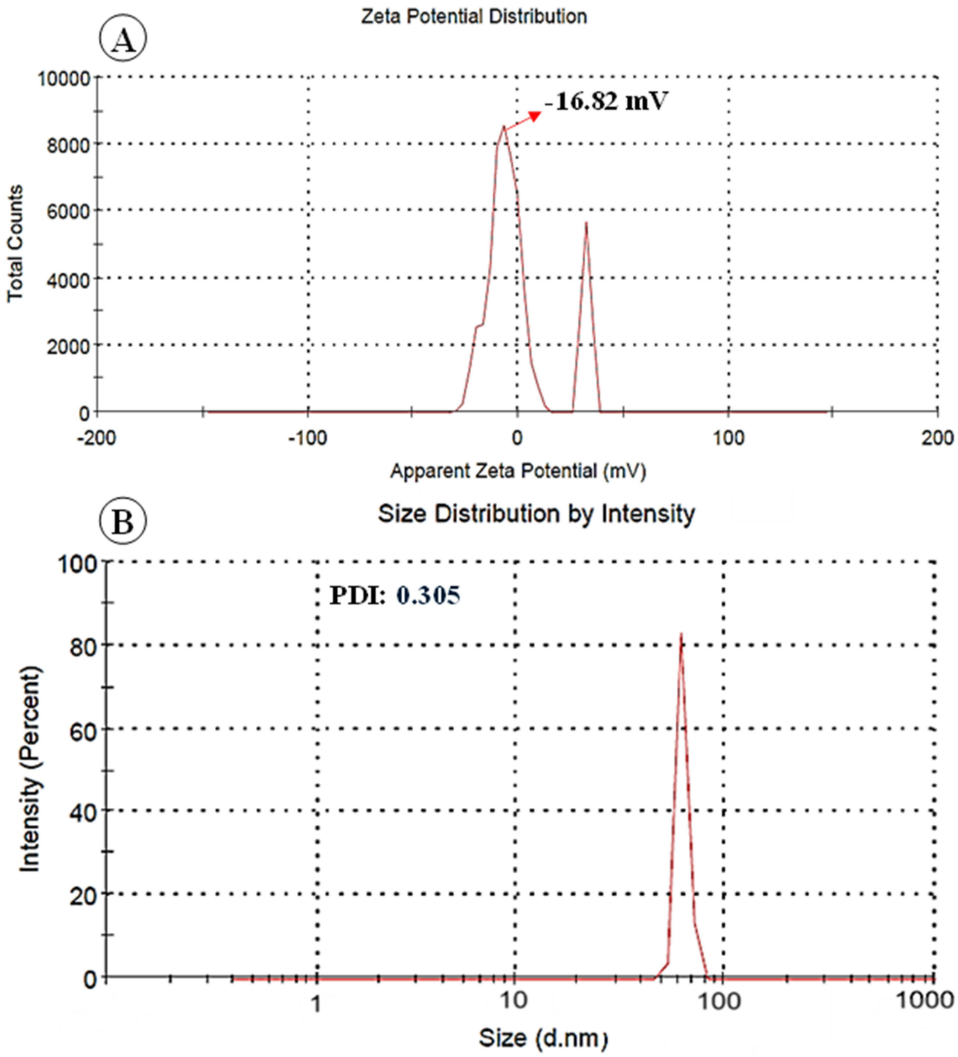

Figure 5 DLS analysis of 6-gingerol loaded MgO NPs, (**A**) zetapotential analysis of Gi-MgO NPs, and (**B**) particle size distribution intensity of Gi- Mg NPs.

Figures 7A–C and 8A. Gi-Mg NPs and 6-gingerol cause cytotoxicity in a pattern that depends on concentration. For 6-gingerol compound cells, the maximal cytotoxic level was 68.85% (IC_{50} = 29.12 µg/mL), whereas for Gi-Mg NPs, it was 82.0% (IC_{50} = 16.48 µg/mL) (Figure 8b). Biosynthetic approaches, which use plant-based materials and associated biocomponents, are an ecologically sound way to synthesize a range of metal and metal oxide nanoparticles (NPs) with changeable form and size. Strong anticancer effects were demonstrated by ZnO and curcumin, both separately and together. Consequently, curcumin-loaded ZnO was evaluated in rhabdomyosarcoma (RD) cell lines. Excellent toxicity against RD cell lines and mild toxicity towards normal cell lines were demonstrated by spherical ZnO-curcumin NPs.[80] Compared to *Papaver somniferum* leaf extract, ZnO NPs exhibited greater effects on THP-1 cells, with inhibitions of 77.33% (IC_{50} = 22.76 µg/mL) compared to 89.67% (IC_{50} = 16.42 µg/mL) for ZnO NPs.[81]

To determine the effectiveness of Gi-MgO NPs and 6-gingerol in preventing cell proliferation. Assays using AO/EtBr staining were used to quantify apoptotic cell death. First, apoptotic cells treated with 6-gingerol extract and Gi-MgO NPs underwent morphological changes in THP-1 cells; the resulting images are displayed in Figure 7D–I. The interpretation of AO/EtBr staining yielded that the Gi-MgO NPs and 6-gingerol (Figures 7E and F) were stained with EtBr (yellow-orange color), which stipulates dead cells, as seen in Figures 7H and I. AO (green), which denotes live cells, was used to stain the control, untreated THP-1 cells. Here, we effectively concluded a second experiment to look into the possible inductive impact of 6-gingerol and Gi-MgO NPs on apoptosis. Thereafter, tagging the genetic material of treated THP-1

https://doi.org/10.2147/IJN.S531933

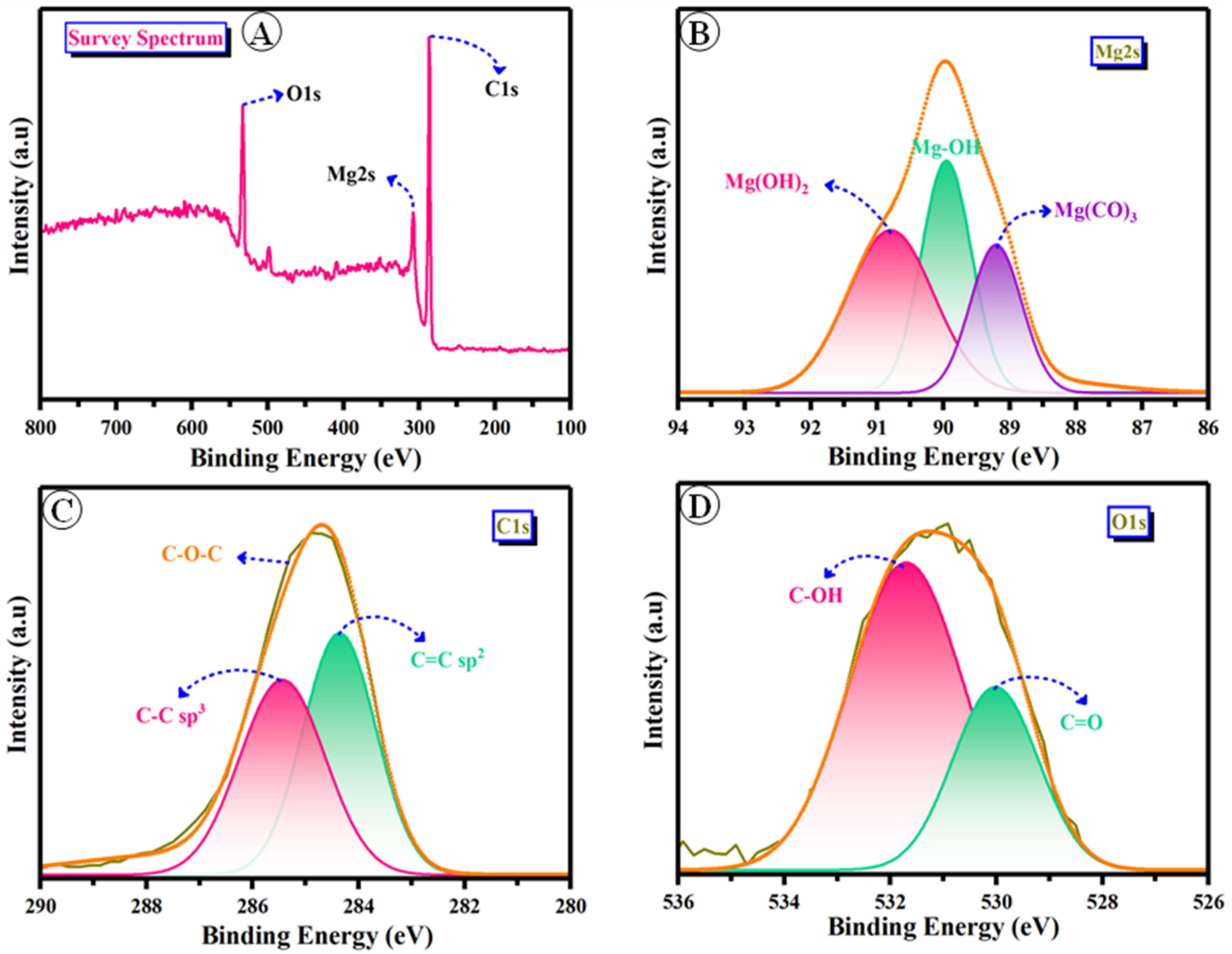

Figure 6 XPS analysis of 6-gingerol loaded MgO NPs. (**A**) XPS survey spectrum, (**B**) Mg-2s, (**C**) C-1s, and (**D**) O-1s.

cells with PI, the quantity of DNA during the sub-G1 phase was measured by flow cytometry (Figure 7J and L). The findings of this study showed that, as shown in Figures 8C and D, the percentage of THP-1 cells treated with Gi-MgO NPs escalated from 5.83 to 30.09%, and the percentage of cancer cells treated with 6-gingerol extract in the sub-G1 phase increased from 6.40 to 33.63%. The MTT assay was used to confirm that NPs caused apoptosis in human brain tumor (U87) cells in a dose-dependent manner in a prior study.[82]

Similarly, NPs that were synthesized via co-precipitation were applied to the human leukemic cell line K562. According to Goorabjavari et al[83] the findings showed that NPs were harmless for normal lymphocyte cells but inhibited the growth of K562 cells. There is no toxicity accorded by NPs treated and normal fibroblast cell lines[81,84] and furthermore, their results show that the percentage of cancer cells treated with *P. somniferum* leaf extract in the sub-G1 phase rose from 2.03 to 27.47%, while the percentage of THP-1 cells treated with NPs increased from 2.03 to 34.59%. In summary, the current study's findings indicate that 6-gingerol and Gi-MgO NPs inhibit proliferation by inducing apoptosis in THP1 cells.

Mechanism of Antitumor Action of 6-Gingerol

6-Gingerol enters cells passively and induces anticancer effects via the ROS-mediated PI3K/Akt/mTOR pathway, independent of autophagy. It overexpresses p21, a G2/M phase regulator, which suppresses cyclin B1 and CDC25A, instigating cell cycle apprehension and apoptosis. Additionally, 6-gingerol disrupts the mitochondrial membrane potential, causing dysregulation of Bcl-2 and upregulation of proapoptotic proteins like Bax, PARP, and cytochrome c. This

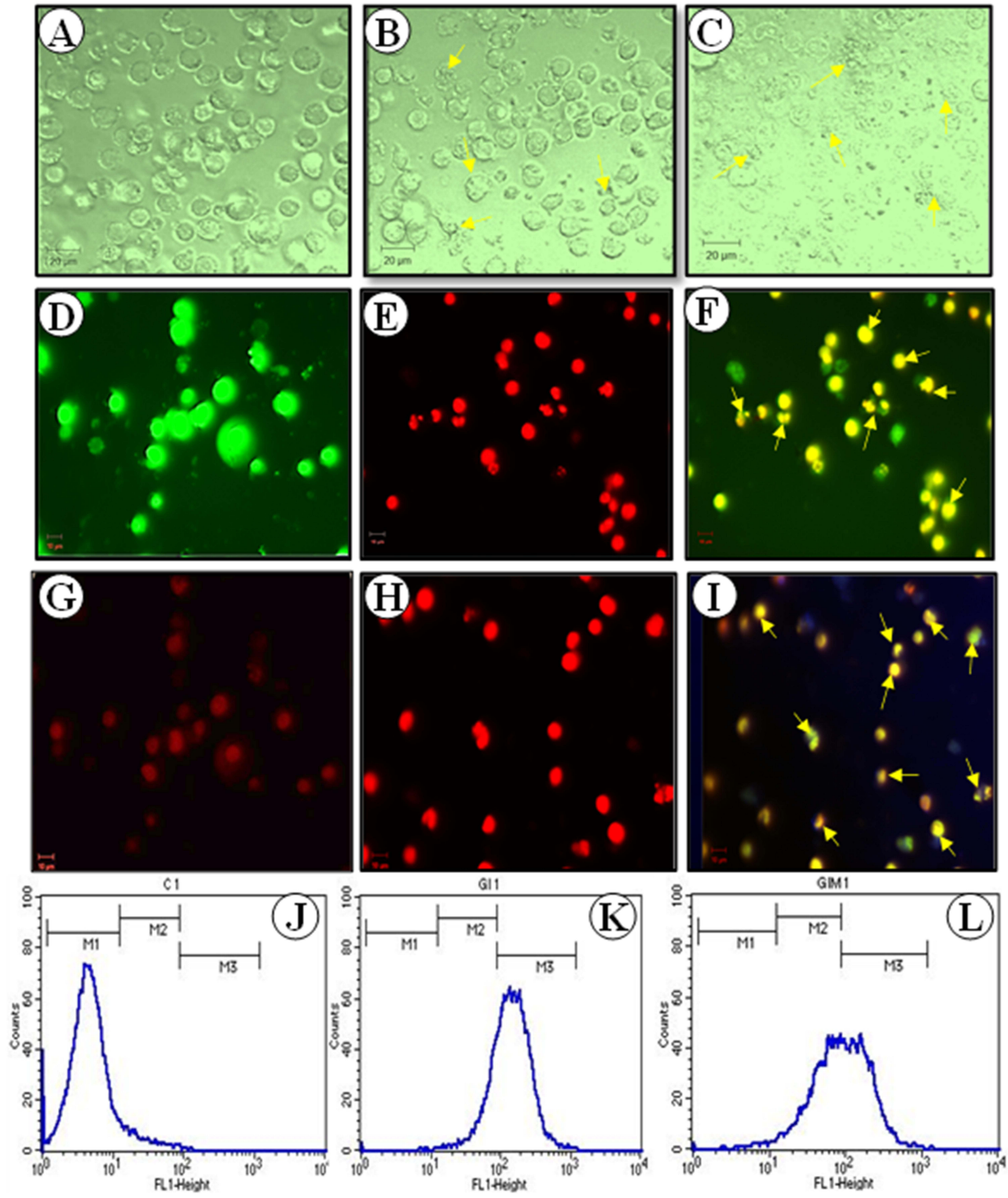

Figure 7 Anticancer evaluation of 6-gingerol loaded MgO NPs. (**A**) control THP-1 cells, (**B**) 6-gingerol treated cells (**C**) Gi-MgO NPs treated cells. (**D**–**I**) Acridine Orange and ethidium bromide (AO/EtBr) stained cells (**D** and **G**) controls, (**E** and **F**) 6-gingerol treated cells, (**H** and **I**) Gi-MgO NPs treated cells (fluorescence images scale bars were 10 μm). (**J**–**L**) Following cell treatment, assessment of apoptosis using flow cytometry. (**J**) Control, (**K**) 6-gingerol, and (**L**) Gi-MgO NPs. The figure of the apoptotic rate in malignant cells after 24 hours of treatment with 6-gingerol and Gi-MgO NPs at IC_{50} concentrations.

https://doi.org/10.2147/IJN.S531933

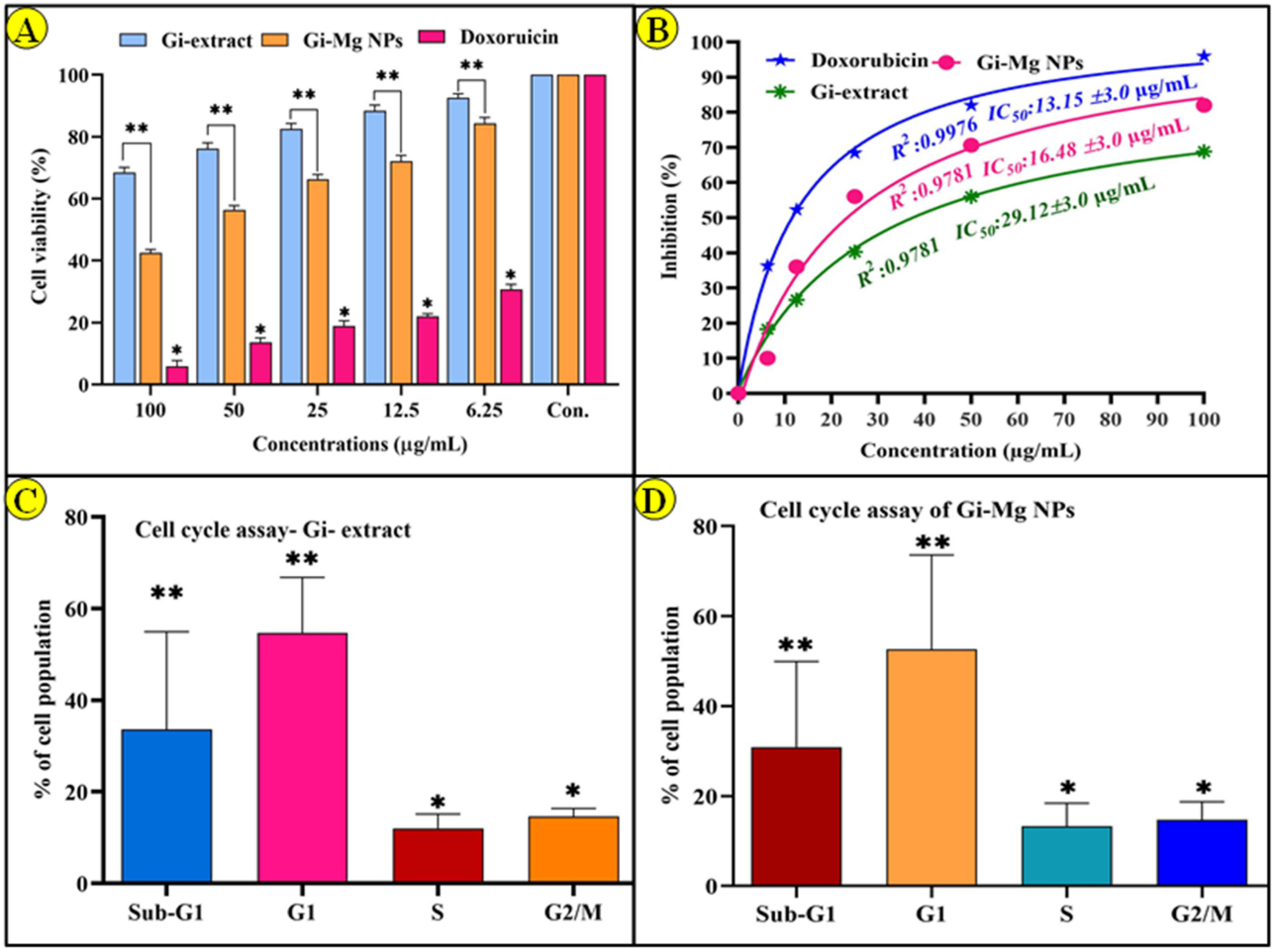

Figure 8 Anticancer activity of 6-gingerol loaded MgO NPs, (**A**) % of cell viability treated with 6-gingerol (Gi-extract), and Gi-Mg NPs. (**B**) cytotoxicity test demonstrating the (IC_{50}) values of Doxorubicin's Gi-MgO NPs, and Gi-extract on THP1 cells; the data were analyzed using nonlinear regression (curve fit) suppression of dosage response. (**C** and **D**) Bar diagram representing the cell distribution in the subG1, G0/G1, S and G2/M phases for THP-1 cells treated with 6-gingerol and Gi-MgO NPs (100 µg/mL). Data shows mean ± standard deviation (n = 3). Asterisk (*, **) shows a substantial variation between treatments in comparison to control (*P < 0.005*).

triggers apoptosis through the mitochondrial pathway. It also increases ROS levels, enhancing cell death in THP-1 cells. 6-Gingerol decreases MMP-2 and MMP-9 levels, downregulates N-cadherin, and increases E-cadherin, inhibiting cellular migration (Figure 9).[85,86] These mechanisms suggest its potential as a therapeutic agent against cancer.

Antioxidant Inhibitory Ability

The potential medical and industrial applications of MgO NPs antioxidant inhibitory action have excited the curiosity of researchers. Due to their unique characteristics, MgO NPs are particularly effective at scavenging reactive oxygen species (ROS) and safeguarding cells from oxidative stress. Standard ascorbic acid and Mg NPs loaded with 6-gingerol have been used to evaluate the scavenging capacity of DPPH results displayed in Figure 10A. For calculating the IC_{50} values, or the sample concentration required to generate 50% of free radicals, regression models for the Gi-MgO NPs amounts from the percentage suppression of the production of free radicals were produced. A lower IC_{50} value corresponds with increased antioxidant activity. The following is the inhibition percentage that was obtained in discrete concentration domains (20–100 µg/mL) at 9.78 ± 2.01, 18.72 ± 1.45, 33.82 ± 1.98, 45.52 ± 2.19, and 69.82 ± 1.64%. Ascorbic acid inhibition percentages are shown to be 18.44 ± 1.64, 28.33 ± 1.63, 46.25 ± 1.82, 56.82 ± 1.68, and 78.40 ± 2.34%, On the other hand, Gi-Mg NPs had an IC_{50} value of 32.14 µg/mL. This study confirmed that 6-gingerol-loaded Mg NPs increased antioxidant activity in a dose-dependent manner. Likewise, the results of Ali et al[87] showed that the MgO NPs produced from *Magnolia champaca* extract had 68.9% of DPPH activity at 120 µg/mL and 13.78% at 20 µg/

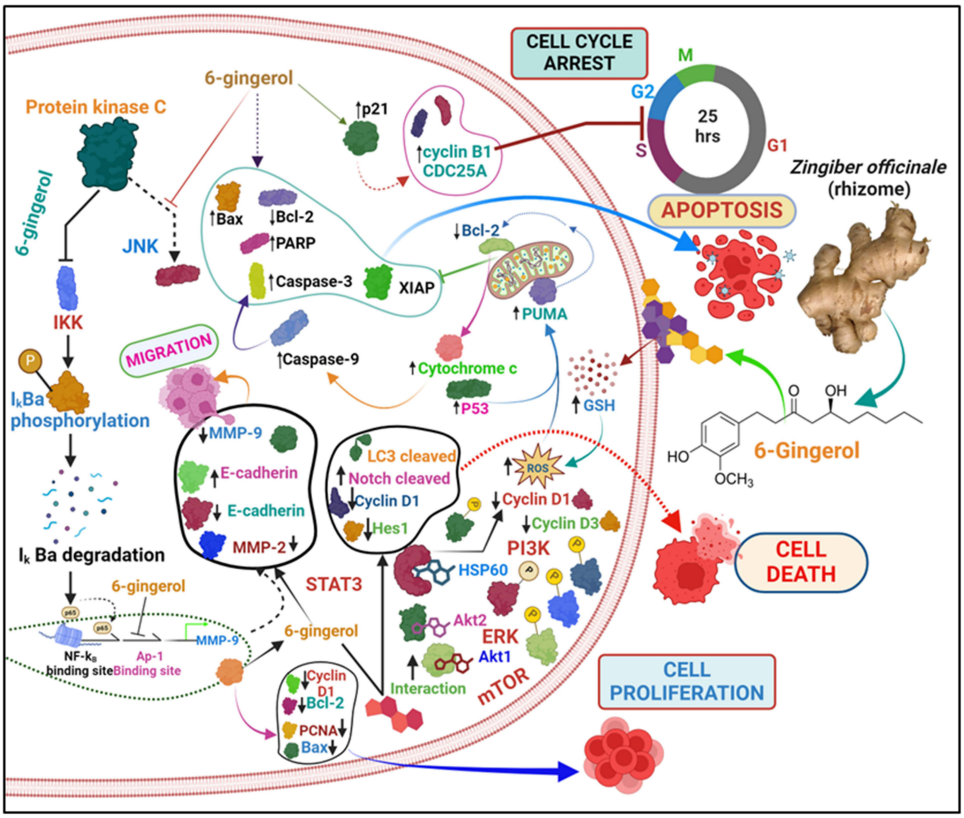

Figure 9 The schematic shows the anticancer mechanisms of 6-gingerol. It influences multifarious proteins and cellular processes rapt in cancer development, such as protein regulation (↑ for activation, ↓ for inhibition) and process induction (→) or repression (⊣). Key proteins and pathways include ERK, Akt, Hes1, HSP60, IKK, IκBα, JNK, LC3, MMP-2, MMP-9, NF-κB, Notch, PI3K, PUMA, STAT3, and XIAP. These molecular interactions suggest 6-gingerol's potential anticancer properties. Developed with BioRender.com (As of July 17, 2024).

mL. In dose-mediated action, the resulting nanoparticles' DPPH property is observed to be greater.[88] Additionally, the Gi-Mg NPs demonstrated a greater ratio of inhibition with an elevated ratio of DPPH scavenging traits when compared to the control.

However, in contrast to traditional ascorbic acid, it was shown that Gi-MgO NPs (20–100 µg/mL) reduced the ABTS* scavenging activity. The findings indicate that, at 100 µg/mL (78.16 ± 1.38%), the Gi-MgO NPs loaded with 6-gingerol had the maximum concentration of free radicals. Other concentrations were found at 80 µg/mL (63.56 ± 1.53%), 60 µg/mL (56.78 ± 1.71%), 40 µg/mL (40.17 ± 1.53%), and 20 µg/mL (31.64 ± 1.91%). The IC_{50} value of Gi-MgO NPs was 26.82 µg/mL. Whereas, ascorbic acid inhibits 86.24 ± 1.27% at 100 µg/mL. In light of the data, Gi-MgO NPs have been found to provide dose-dependent antioxidant capacity (Figure 10B). Furthermore, the relationship between these elements and metals is more thoroughly examined, as are the kinds of characteristics that may cause challenges for nanoparticles but have not yet been documented. We are presenting the first-ever findings on the antioxidant characteristics of MgO NPs loaded with 6-gingerol. These results include a considerable increase in the proportion of antioxidant properties and scavenging ability.

Anti-Inflammatory Effects of Gi-Mg NPs

As a natural defense mechanism, inflammation helps the body prevent infections from spreading. Inflammation is the body's intricate response to injury or disease. Indications of the inflammatory process inside the affected area include swelling, reddening, and discomfort. The inflammation is mediated by a number of mediators and cytokines. While inflammation serves as a natural defense mechanism, both acute and chronic inflammatory responses are the root cause of most human disorders, including diabetes and cancer.[89] Based on the current study, anti-inflammatory capabilities, egg albumin denaturation, and nanoparticles' ability to inhibit protein are determined.[90,91] The ability of 6-gingerol-loaded

https://doi.org/10.2147/IJN.S531933

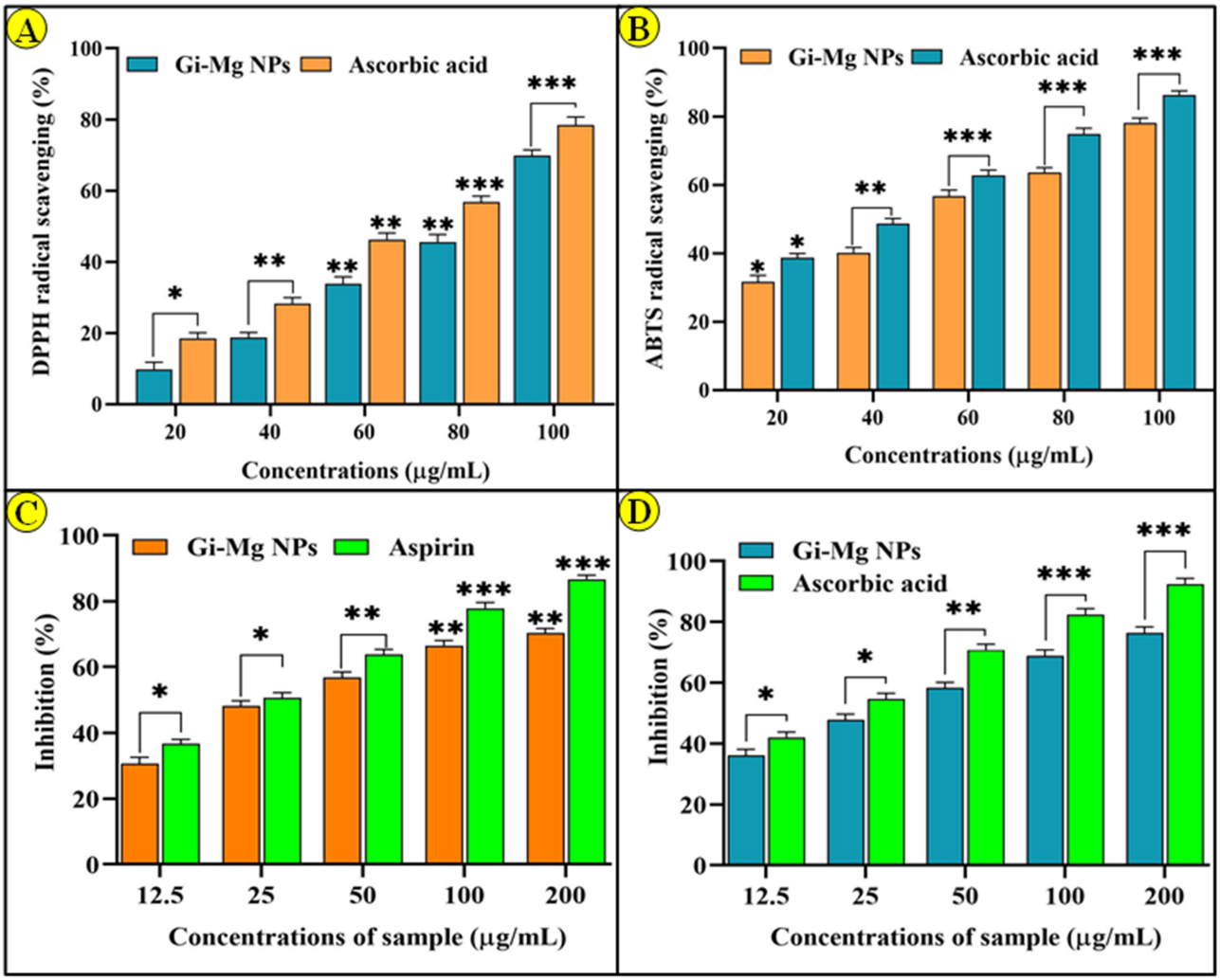

Figure 10 6-gingerol loaded MgO NPs revealed antioxidant assay, (**A**) DPPH and (**B**) ABTS. Anti-inflammatory activity of 6-gingerol and Gi-MgO NPs (**C**) Protein denaturation assay, and (**D**) Membrane stabilizing activity. Data shows mean ± standard deviation (n = 3). Asterisk (*, **, ***) shows a substantial difference between treatment groups and control groups ($P < 0.005$).

Mg NPs to inhibit temperature-stimulated egg albumin denaturation was assessed at 12.5, 25, 50, 100, and 200 µg/mL (Figure 10C). According to this study, aspirin exhibits 9.2% at 20 µg/mL and 82.30% at 120 µg/mL concentration, while 36.64% at 12.5 µg/mL and 86.61% at 200 µg/mL, when compared to standard similar results were obtained by 6-gingerol-loaded MgO NPs. These findings suggest that Gi-MgO NPs could inhibit the protein denaturation of albumin in a concentration-dependent process. Furthermore, in comparison to the reference standard, it was discovered that the in vitro anti-inflammatory efficiency of HRBC membrane stability decreased at higher sample levels. It was discovered that the absorbance of the Gi-MgO NPs was greater than that of the standard. When measured against the 6-gingerol-loaded MgO NPs, a notable anti-inflammatory impact was seen. At doses of 12.5–200 µg/mL, the Gi-MgO NPs demonstrated a significant proportion of protection and membrane stability, ranging from 36.14% to 76.40% (Figure 10D). According to Imath et al,[92] in a membrane stability investigation, the Ag-NPs made from *Fioria vitifolia* leaf water extract showed the next-highest level of protection, ranging from 25% to 75% at 50–250 µg/mL, and the highest percentage of albumin denaturation, ranging from 75% at 250 µg/mL. At concentrations ranging from 20 to 120 µg/mL, *M. champaca* extract-assisted MgO NPs effectively inhibited albumin's protein denaturation in a concentration-mediated process.[87] The study demonstrates the possible uses of 6-gingerol-loaded Mg NPs in medicine by providing a comprehensive analysis of their anti-inflammatory properties. Through a comparison of their effectiveness with aspirin, the study provides a reliable baseline. However, further research is necessary to fully comprehend Gi-MgO

NPs methods of action, especially in light of how they affect pro-inflammatory mediators and whether they have any negative side effects. Though encouraging, there are concerns about the immunogenicity, cytotoxicity, and accumulating risk of Mg in Gi-MgO NPs. Even though Gi-Mg NPs appear to have potential for anti-inflammatory treatment, more investigation is necessary to guarantee their safe and efficient application in clinical settings.

Molecular Docking Analysis

The human SIRT2 protein is a crucial druggable target for anti-cancer drug discovery. SIRT2 is one of seven human sirtuins proteins. It is a cytoplasmic enzyme that deacetylates α-tubulin and histones, as well as a lot of other transcriptional factors like NF-κB and p53. The 6-gingerol complex exhibited a conventional H bond interaction with the amino acids of LEU A:212 and ALA A:33, a C, H- bond interaction with Gly A:32 and Gly A:209, and a pi-alkyl interaction with Ile A:180, Phe A:67, and Val A:214 of the human Sirt2 protein, with a docking score of −7.0 kcal/mol. Figure 11A and **B** showed that the Sirt2 protein and 6-gingerol complex engage in both 3D and 2D interactions. The standard drug Tenovin-3 had an H-bond interaction with GLY A:89, a Pi-Pi T-shaped interaction with Phe A:91, and a Pi-Alkyl interaction with the Leu A:154 and

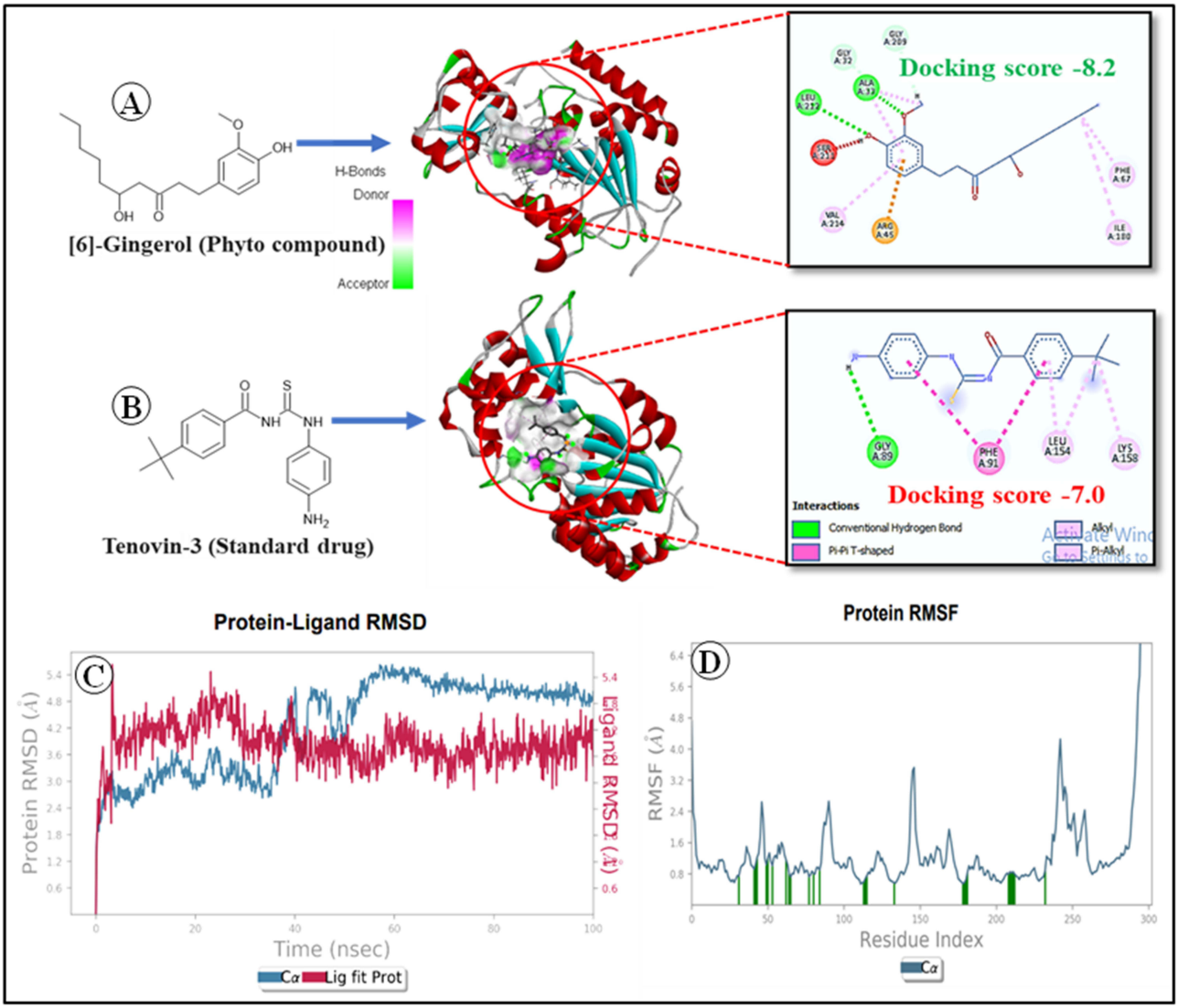

Figure 11 Molecular docking and MD simulations of 6-gingerol, (**A**) 3D and 2D interaction of Sirt2 protein and 6-gingerol complex, (**B**) 3D and 2D interaction of Sirt2 protein and Tenovin-3 complex, (**C**) 6-gingerol and Sirt2 protein complex's root mean square deviation (RMSD) profile as determined by MD simulation, and (**D**) Root mean square fluctuation (RMSF) profile of human Sirt2 protein as determined by MD simulation.

https://doi.org/10.2147/IJN.S531933

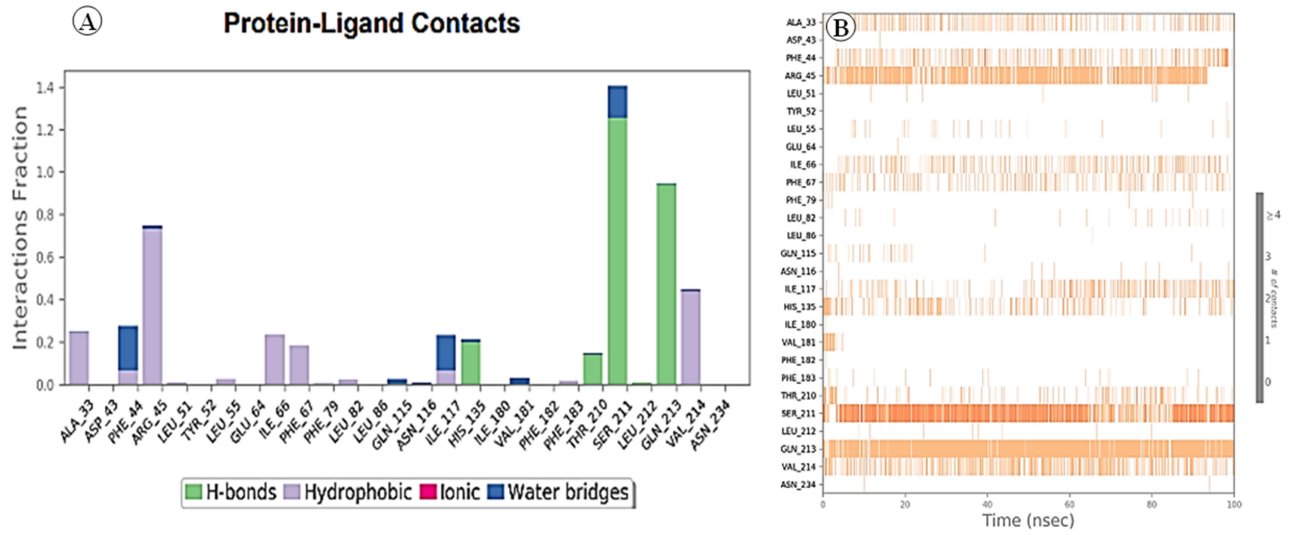

Figure 12 Profile of protein-ligand interactions of important interacting amino acids during 6-gingerol and Sirt2 protein complex MD simulation (**A**), and a timeline depicting how the ligand interacts with the amino acids in the Sirt2 protein (**B**).

Lys A:158 amino acids of the human Sirt2 protein. The docking score for these interactions was −8.2 kcal/mol, and the standard drug Tenovin-3 exhibited −7.0 kcal/mol.

Molecular Dynamics Simulation Results

6-gingerol was subjected to MD simulation to analyze the stability of the ligand in the active binding domain of the intended protein. We observed that 6-gingerol exhibited stability, with minimal fluctuations in its conformation throughout the simulation time. The molecular dynamics simulation for 100 ns was subjected to evaluate the stability and interactions evaluated using statistical parameters harnessed from RMSD, RMSF, and protein-ligand interactions fraction. We analyzed the fluctuation of C-alpha residues and ligands using the RMSD plot, as shown in Figure 11C. It shows that the protein-ligand complex's RMSD value was less than 5.5 Å. In the first 40 ns of the dynamic simulation, the protein's RMSD values rose from 2.4 ns to 4.2 ns. From 45 ns to 50 ns, the RMSD decreased from 4.8 ns to 4.2 ns. In the first 50 ns of the simulation, the complex was stable at 5 Å, after 50 ns of the simulation, the complex increased up to 5.5 Å. After 50 ns, it increased from 2.4 ns to 4.2 ns to 5.4 ns. This suggests that the ligand maintained a steady interaction with minimal fluctuations in the protein's active site. Figure 11D shows the RMSF plot of the protein structure. The RMSF values of the Sert2 protein residues vary between 0.8 Å and 4 Å. This suggests that the thermal motion does not cause any local alterations in the protein chain. Figure 12A shows the H-bond interaction of the protein-ligand complex during the simulation time. It shows that the 6-Gingerol compound had stable H-bond interaction at residues of HIS 135, THR 210, SER 211, and GLN 213 at a maximum of 90% of the simulation time. The 6-gingerol compound also had hydrophobic interactions at residues with ALA 33, ARG 45, ILE 66, PHE 67, and VAL 214 for a maximum of 90% of the simulation time. Figure 12B shows that gingerol has a stable hydrogen bond interaction with the ARG:45, SER:211, and GLN:213 amino acid residues of the human Sirt2 protein. During the simulation, the number of H-bonds between the protein and ligand ranges from 0 to 4. The MD simulation outcome suggested that the protein-ligand complex was fairly stable during the simulation.

Conclusion and Perspectives

6-Gingerol and its loaded Mg NPs have the ability to suppress cell migration and proliferation, trigger cell cycle arrest and death, and alter important signalling entailed in the initiation and metastasis. Gi-MgO NPs are characterized by FT-IR spectroscopy, XRD, DLS, SEM-EDX, TEM, and XPS investigations. Findings from these investigations showed that the biosynthesized Gi-MgO NPs range in size from 12.5 to 57.6 nm and are crystalline, spherical, and well-dispersed. In light of this, we suggest the following next paths for Gi-MgO NP research:

i. To evaluate Gi-MgO NPs antiangiogenic, proapoptotic, and antimetastatic effects in a genre of cancer cell types and animal models, as well as the primary molecular targets and regulators implicated in these activities.
ii. Investigate Gi-MgO NP's involvement in regulating the cellular stress response and mitochondrial function by looking at its binding mechanism and interaction locations in cancer cells.
iii. To assess Gi-MgO NPs impact on the immune system and tumour microenvironment, as well as to maximize the antitumor effect in THP1 via the PI3K/Akt/mTOR pathway by dose optimization and mode of administration.
iv. To investigate the impact of Gi-MgO NPs on oncogenes and tumour suppressor genes as well as the epigenetic control of DNA methylation and gene expression in THP1 cells.

All things considered, the evidence points to the good anticancer, antioxidant, and anti-inflammatory properties of magnesium NPs laden with 6-gingerol. To determine the molecular mechanisms of action of Gi-MgO NPs in various cancer types and stages, as well as their pharmacokinetics, bioavailability, and safety in individuals, more research is required. To increase its effectiveness and lower its toxicity, Gi-MgO NPs synergistic or additive actions with conventional chemotherapeutic drugs or other natural chemicals need to be investigated. The stability and bioactivity of 6-gingerol-loaded MgO NPs could be enhanced in vivo by creating innovative formulations or administration methods. To fully realize the promise of Gi-MgO NPs as a novel anticancer agent derived from ginger, further research is therefore necessary. These findings demonstrate the notability of green technology in the production of nanoparticles as well as its potential for use in biomedicine and disease prevention in the future.

Data Sharing Statement

The data presented in this study are available on request from the corresponding author.

Ethical Aspects

There is no ethical approval needed to accomplish this work.

Acknowledgments

The authors would like to thank IIISM and NRC for providing the specialized resources to characterize the nanoparticles and conduct the research. **C.K**. sincerely thanks the BRIN for their support through the visiting researcher fellowship. The authors express their sincere appreciation to the Ongoing Research Funding program, (ORF-2026-48), King Saud University, Riyadh, Saudi Arabia.

Author Contributions

All authors made a significant contribution to the work reported, whether that is in the conception, study design, execution, acquisition of data, analysis, and interpretation, or in all these areas; took part in drafting, revising, or critically reviewing the article; gave final approval of the version to be published; have agreed on the journal to which the article has been submitted; and agree to be accountable for all aspects of the work.

Disclosure

The authors report no conflicts of interest in this work.

References

1. Lin L, Li Z, Yan L, Liu Y, Yang H, Li H. Global, regional, and national cancer incidence and death for 29 cancer groups in 2019 and trends analysis of the global cancer burden, 1990–2019. *J Hematol Oncol*. 2021;14(1):1–24. doi:10.1186/s13045-021-01213-z
2. Bray F, Laversanne M, Sung H, et al. Global cancer statistics 2022: GLOBOCAN estimates of incidence and mortality worldwide for 36 cancers in 185 countries. *CA Cancer J Clin*. 2024;74:1–35. doi:10.3322/caac.21834
3. Debela DT, Muzazu SG, Heraro KD, et al. New approaches and procedures for cancer treatment: current perspectives. *SAGE Open Med*. 2021;9:20503121211034366. doi:10.1177/20503121211034366
4. Ferlay J, Steliarova-Foucher E, Lortet-Tieulent J, et al. Cancer incidence and mortality patterns in Europe: estimates for 40 countries in 2012. *Eur J Cancer*. 2013;49:1374–1403. doi:10.1016/j.ejca.2012.12.027

5. Basak D, Arrighi S, Darwiche Y, Deb S. Comparison of anticancer drug toxicities: paradigm shift in adverse effect profile. *Life*. 2021;12:48. doi:10.3390/life12010048
6. Dallavalle S, Dobričić V, Lazzarato L, et al. Improvement of conventional anti-cancer drugs as new tools against multidrug-resistant tumors. *Drug Resist Updat*. 2020;50:100682. doi:10.1016/j.drup.2020.100682
7. Holohan C, Van Schaeybroeck S, Longley DB, Johnston PG. Cancer drug resistance: an evolving paradigm. *Nat Rev Cancer*. 2013;13:714–726. doi:10.1038/nrc3599
8. Nedungadi D, Binoy A, Pandurangan N, Pal S, Nair B, Mishra N. 6-Shogaol induces caspase-independent paraptosis in cancer cells via proteasomal inhibition. *Exp Cell Res*. 2018;364:243–251. doi:10.1016/j.yexcr.2018.02.018
9. Mashhadi NS, Ghiasvand R, Askari G, Hariri M, Darvishi L, Mofid MR. Anti-oxidative and anti-inflammatory effects of ginger in health and physical activity: review of current evidence. *Int J Prev Med*. 2013;4:36.
10. Wang X, Shen Y, Thakur K, et al. Antibacterial activity and mechanism of ginger essential oil against *Escherichia coli* and *Staphylococcus aureus*. *Molecules*. 2020;25(17):3955. doi:10.3390/molecules25173955
11. Osaro-Matthew RC, Ire FS, Frank-Peterside N. Screening of actinomycetes from turmeric (*Curcuma longa* L.) and ginger (*Zingiber officinale*) rhizosphere for antifungal activity. *J Adv Microbiol*. 2020;20:18–28. doi:10.9734/JAMB/2020/v20i230214
12. Ahmed SHH, Gonda T, Hunyadi A. Medicinal chemistry inspired by ginger: exploring the chemical space around 6-gingerol. *RSC Adv*. 2021;11 (43):26687–26699. doi:10.1039/D1RA04227K
13. Chatupheeraphat C, Nantasenamat C, Deesrisak K, Roytrakul S, Anurathapan U, Tanyong D. Bioinformatics and experimental studies of anti-leukemic activity from 6-gingerol demonstrate its role in p53 mediated apoptosis pathway. *Excli J*. 2020;19:582. doi:10.17179/excli2019-2008
14. Karatay KB, Kılçar AY, Derviş E, Müftüler FZB. Radioiodinated ginger compounds (6-gingerol and 6-shogaol) and incorporation assays on breast cancer cells. *Anticancer Agents Med Chem*. 2020;20(9):1129–1139. doi:10.2174/1871520620666200128114215
15. Damare R, Engle K, Kumar G. Targeting epidermal growth factor receptor and its downstream signaling pathways by natural products: a mechanistic insight. *Phytother Res*. 2024;38(5):2406–2447. doi:10.1002/ptr.8166
16. Manatunga DC, De Silva RM, De Silva KMN, Wijeratne DT, Malavige GN, Williams G. Fabrication of 6-gingerol, doxorubicin and alginate hydroxyapatite into a bio-compatible formulation: enhanced anti-proliferative effect on breast and liver cancer cells. *Chem Cent J*. 2018;12 (1):1–13. doi:10.1186/s13065-018-0482-6
17. Kazazi I, Ashrafi F, Malekloo M. Synthesis of gingerol-loaded Uio-66 nanoparticles and its anti-cancer effect against gastric cancer cell line (AGS). *Mol Biol Rep*. 2023;50(4):3503–3513. doi:10.1007/s11033-022-07667-9
18. Fakhar Ud Din FU, Aman W, Ullah I, Qureshi O, Mustapha O, Shafique S. Effective use of nanocarriers as drug delivery systems for the treatment of selected tumors. *Int J Nanomed*. 2017;12:7291–7309. doi:10.2147/IJN.S146315
19. Cao Y, Khan A, Mirzaei H, et al. Investigations of adsorption behavior and anti-cancer activity of curcumin on pure and platinum-functionalized B12N12 nanocages. *J Mol Liq*. 2021;334:116516. doi:10.1016/j.molliq.2021.116516
20. Chen J, Wu L, Lu M, Lu S, Li Z, Ding W. Comparative study on the fungicidal activity of metallic MgO nanoparticles and macroscale MgO against soilborne fungal phytopathogens. *Front Microbiol*. 2020;11:365. doi:10.3389/fmicb.2020.00365
21. Yang Y, Liu J, Zhou X. A CRISPR-based and post-amplification coupled SARS-CoV-2 detection with a portable evanescent wave biosensor. *Biosens Bioelectron*. 2021;190:113418. doi:10.1016/j.bios.2021.113418
22. Spoiala A, Ilie C-I, Motelica L, et al. Smart magnetic drug delivery systems for the treatment of cancer. *Nanomaterials*. 2023;13(5):876. doi:10.3390/nano13050876
23. Malik JA, Ansari JA, Ahmed S, Khan A, Ahemad N, Anwar S. Nano-drug delivery system: a promising approach against breast cancer. *Ther Deliv*. 2023;14(5):357–381. doi:10.4155/tde-2023-0020
24. Singh S, Banerjee R, Pal K. Emerging trends in biodegradable polymer-metal nanoconjugates for cancer therapeutics. *Eur Polym J*. 2024;207:112835. doi:10.1016/j.eurpolymj.2024.112835
25. Mathur P, Kumawat M, Nagar R, Singh R, Daima HK. Tailoring metal oxide nanozymes for biomedical applications: trends, limitations, and perceptions. *Anal Bioanal Chem*. 2024;1–20. doi:10.1007/s00216-024-05416-4
26. Li Y, Song K, Cao Y, Peng C, Yang G. Keratin-templated synthesis of metallic oxide nanoparticles as MRI contrast agents and drug carriers. *ACS Appl Mater Interfaces*. 2018;10:26039–26045.
27. Singh KR, Nayak V, Singh J, Singh AK, Singh RP. Potentialities of bioinspired metal and metal oxide nanoparticles in biomedical sciences. *RSC Adv*. 2021;1:24722–24746. doi:10.1039/D1RA04273D
28. Nejati M, Rostami M, Mirzaei H, et al. Green methods for the preparation of MgO nanomaterials and their drug delivery, anti-cancer and anti-bacterial potentials: a review. *Inorg Chem Commun*. 2022;136:109107. doi:10.1016/j.inoche.2021.109107
29. Martin V, Bettencourt AF, Fernandes MH, et al. Green synthesis of Zn–Mg layered hydroxide nanoparticles with surface-mediated antioxidant and anti-inflammatory activity. *J Surf*. 2024;46:104037. doi:10.1016/j.surfin.2024.104037
30. Nagchowdhury P, Krishna M, Patra CR R, Javed, JT, Chen, AT, Khalil. Biomedical applications of magnesium oxide nanoparticles. In: *Nanomaterials for Biomedical and Bioengineering Applications* 1. Singapore: Springer Nature Singapore;2024:97–132. doi:10.1007/978-981-97-0221-3_5
31. Abdel-Aziz MM, Emam TM, Elsherbiny EA. Bioactivity of magnesium oxide nanoparticles synthesized from cell filtrate of endobacterium *Burkholderia rinojensis* against *Fusarium oxysporum*. *Mater Sci Eng C*. 2020;109:110617. doi:10.1016/j.msec.2019.110617
32. Anicic N, Vukomanovic M, Koklic T, Suvorov D. Fewer defects in the surface slows the hydrolysis rate, decreases the ROS generation potential, and improves the non-ROS antimicrobial activity of MgO. *Small*. 2018;14:1800205. doi:10.1002/smll.201800205
33. Anand KV, Anugraga AR, Kannan M, Singaravelu G, Govindaraju K. Bio-engineered magnesium oxide nanoparticles as nano-priming agents for enhancing seed germination and seedling vigor of green gram (*Vigna radiata* L.). *Mater Lett*. 2020;271:127792. doi:10.1016/j.matlet.2020.127792
34. Verma SK, Nisha K, Panda PK, et al. Green synthesized MgO nanoparticles infer biocompatibility by reducing in vivo molecular nanotoxicity in embryonic zebrafish through arginine interaction elicited apoptosis. *Sci Total Environ*. 2020;713:136521. doi:10.1016/j.scitotenv.2020.136521
35. Maji J, Pandey S, Basu S. Synthesis and evaluation of antibacterial properties of magnesium oxide nanoparticles. *Bull Mater Sci*. 2020;43:1–10. doi:10.1007/s12034-019-1963-5
36. Tang ZX, Lv BF. MgO nanoparticles as antibacterial agent: preparation and activity. *Braz J Chem Eng*. 2014;31:591–601. doi:10.1590/0104-6632.20140313s00002813

37. El-Sayyad GS, Mosallam FM, El-Batal AI. One-pot green synthesis of magnesium oxide nanoparticles using *Penicillium chrysogenum* melanin pigment and gamma rays with antimicrobial activity against multidrug-resistant microbes. *Adv Powder Technol*. 2018;29:2616–2625. doi:10.1016/j.apt.2018.07.009
38. Khan A, Shabir D, Ahmad P, Khandaker MU, Faruque MRI, Din IU. Biosynthesis and antibacterial activity of MgO-NPs produced from *Camellia sinensis* leaf extract. *Mater Res Express*. 2020;8:015402. doi:10.1088/2053-1591/abd421
39. Castillo IF, Guillén EG, De la Fuente JM, Silva F, Mitchell SG. Preventing fungal growth on heritage paper with antifungal and cellulase-inhibiting magnesium oxide nanoparticles. *J Mater Chem B*. 2019;7:6412–6419.
40. Di DR, He ZZZ, Sun ZQ, Liu J. A new nano-cryosurgical modality for tumor treatment using biodegradable MgO nanoparticles. *Nanomed Nanotechnol Biol Med*. 2012;8:1233–1241. doi:10.1016/j.nano.2012.02.010
41. Krishnamoorthy K, Moon JY, Hyun HB, Cho SK, Kim SJ. Mechanistic investigation on the toxicity of MgO nanoparticles toward cancer cells. *J Mater Chem*. 2012;22:24610–24617.
42. Moeini-Nodeh S, Rahimifard M, Baeeri M, Abdollahi M. Functional improvement in rats' pancreatic islets using magnesium oxide nanoparticles through antiapoptotic and antioxidant pathways. *Biol Trace Elem Res*. 2017;175:146–155. doi:10.1007/s12011-016-0754-8
43. Derakhshankhah H, Nekounam H, Izadi Z, Allahyari Z, Samari M, Samadian H. Fabrication of electroactive nanocomposite based on carbon nanofibers/magnesium oxide nanoparticles for bone tissue engineering. *J Drug Deliv Technol*. 2023;89:105082. doi:10.1016/j.jddst.2023.105082
44. Li J, Khalid A, Verma R, et al. Silk fibroin coated magnesium oxide nanospheres: a biocompatible and biodegradable tool for noninvasive bioimaging applications. *Nanomaterials*. 2021;11:695. doi:10.3390/nano11030695
45. El-Sawy NM, Raafat AI, Badawy NA, Mohamed AM. Radiation development of pH-responsive (xanthan-acrylic acid)/MgO nanocomposite hydrogels for controlled delivery of methotrexate anticancer drug. *Int J Biol Macromol*. 2020;142:254–264. doi:10.1016/j.ijbiomac.2019.09.097
46. Singh AB, Akanksha Singh N, Maurya R, Srivastava AK. Antihyperglycemic, lipid-lowering, and antioxidant properties of [6]-gingerol in *db/db* mice. *Int J Med Med Sci*. 2009;1:536–544.
47. Wagner H, Bladt S. *Plant Drug Analysis: A Thin Layer Chromatography Atlas*. Springer Science & Business Media; 1996:1–369.
48. Maleš Z, Plazibat M, Vundać VB, Žuntar I, Pilepić KH. Thin-layer chromatographic analysis of flavonoids, phenolic acids, and amino acids in some Croatian *Hypericum* taxa. *JPC-J Planar Chromatogr*. 2004;17:280–285. doi:10.1556/JPC.17.2004.4.7
49. Kamaraj C, Naveenkumar S, Kumar RC, Al-Ghanim KA, Natesan K, Priyadharsan A. Ice apple fruit peel assisted bio-synthesis of zinc oxide nanoparticles (ZnO NPs): an anticancer, antimicrobial, and larvicidal applications. *J Drug Deliv Technol*. 2025;105:106585. doi:10.1016/j.jddst.2024.106585
50. Hamza MF, Salih KA, Adel AH, et al. Sulfonic-functionalized algal/PEI beads for scandium, cerium, and holmium sorption from aqueous solutions (synthetic and industrial samples). *Chem Eng J*. 2021;403:126399. doi:10.1016/j.cej.2020.126399
51. Mosmann T. Rapid colorimetric assay for cellular growth and survival: application to proliferation and cytotoxicity assays. *J Immunol Methods*. 1983;65:55–63. doi:10.1016/0022-1759(83)90303-4
52. Gurunathan S, Jeyaraj M, Kang MH, Kim JH. The effects of apigenin-biosynthesized ultra-small platinum nanoparticles on the human monocytic THP-1 cell line. *Cells*. 2019;8:444. doi:10.3390/cells8050444
53. Foudah AI, Shakeel F, Yusufoglu HS, Ross SA, Alam P. Simultaneous determination of 6-shogaol and 6-gingerol in various ginger (*Zingiber officinale* Roscoe) extracts and commercial formulations using a green RP-HPTLC-densitometry method. *Foods*. 2020;9:1136. doi:10.3390/foods9081136
54. Khan I, Pandotra P, Gupta AP, et al. RP-thin layer chromatographic method for the quantification of three gingerol homologs of ultrasonic-assisted fresh rhizome extracts of *Zingiber officinale* collected from North Western Himalayas. *J Sep Sci*. 2010;33:558–563. doi:10.1002/jssc.200900629
55. Zhan K, Xu K, Yin H. Preparative separation and purification of gingerols from ginger (*Zingiber officinale* Roscoe) by high-speed counter-current chromatography. *Food Chem*. 2011;126:1959–1963. doi:10.1016/j.foodchem.2010.12.052
56. Da Silva JA, Sampaio PA, Dulcey LJL, Cominetti MR, Rabello MM, Rolim LA. Preparation and characterization of [6]-gingerol/β-cyclodextrin inclusion complexes. *J Drug Deliv Technol*. 2021;61:102103. doi:10.1016/j.jddst.2020.102103
57. Ramanujam K, Sundrarajan M. Antibacterial effects of biosynthesized MgO nanoparticles using ethanolic fruit extract of *Emblica officinalis*. *Photochem Photobiol B Biol*. 2014;141:296–300. doi:10.1016/j.jphotobiol.2014.09.011
58. Dobrucka R. Synthesis of MgO nanoparticles using *Artemisia abrotanum* herba extract and their antioxidant and photocatalytic properties. *Iran J Sci Technol Trans*. 2018;42:547–555. doi:10.1007/s40995-016-0076-x
59. Coates J. Interpretation of infrared spectra, a practical approach. *Anal Chem*. 2000;12:10815–10837.
60. Taourati R, Khaddor M, Laghzal A, El Kasmi A. Facile one-step synthesis of highly efficient single oxide nanoparticles for photocatalytic application. *Sci Afr*. 2020;8:e00305. doi:10.1016/j.sciaf.2020.e00305
61. Karthik K, Dhanuskodi S, Gobinath C, Prabukumar S, Sivaramakrishnan S. Fabrication of MgO nanostructures and its efficient photocatalytic, antibacterial and anticancer performance. *Photochem Photobiol B Biol*. 2019;190:8–20. doi:10.1016/j.jphotobiol.2018.11.001
62. Wei Y, Salih KA, Rabie K, et al. Development of phosphoryl-functionalized algal-PEI beads for the sorption of Nd (III) and Mo (VI) from aqueous solutions–Application for rare earth recovery from acid leachates. *J Chem Eng*. 2021;412:127399. doi:10.1016/j.cej.2020.127399
63. Pugazhendhi A, Prabhu R, Muruganantham K, Shanmuganathan R, Natarajan S. Anticancer, antimicrobial and photocatalytic activities of green synthesized magnesium oxide nanoparticles (MgONPs) using aqueous extract of *Sargassum wightii*. *Photochem Photobiol B Biol*. 2019;190:86–97. doi:10.1016/j.jphotobiol.2018.11.014
64. Fouda A, Hassan SED, Saied E, Hamza MF. Photocatalytic degradation of real textile and tannery effluent using biosynthesized magnesium oxide nanoparticles (MgO-NPs), heavy metal adsorption, phytotoxicity, and antimicrobial activity. *J Environ Chem Eng*. 2021;9:105346. doi:10.1016/j.jece.2021.105346
65. Safaei GJ, Zahedi S, Javid M, Ghasemzadeh MA. MgO nanoparticles: an efficient, green and reusable catalyst for the one-pot syntheses of 2,6-dicyanoanilines and 1,3-diarylpropyl malononitriles under different conditions. *J Nanostruct*. 2015;5:153–160.
66. Lekota MW, Dimpe KM, Nomngongo PN. MgO-ZnO/carbon nanofiber nanocomposite as an adsorbent for ultrasound-assisted dispersive solid-phase microextraction of carbamazepine from wastewater prior to high-performance liquid chromatographic detection. *J Anal Sci Technol*. 2019;10:25. doi:10.1186/s40543-019-0185-1
67. Hassan SED, Fouda A, Saied E, et al. *Rhizopus oryzae*-mediated green synthesis of magnesium oxide nanoparticles (MgO-NPs): a promising tool for antimicrobial, mosquitocidal action, and tanning effluent treatment. *J Fungi*. 2021;7:372. doi:10.3390/jof7050372

68. Alsharif SM, Salem SS, Abdel-Rahman MA, et al. Multifunctional properties of spherical silver nanoparticles fabricated by different microbial taxa. *Heliyon*. 2020;6:e03943. doi:10.1016/j.heliyon.2020.e03943
69. El-Belely EF, Farag MM, Said HA, et al. Green synthesis of zinc oxide nanoparticles (ZnO-NPs) using *Arthrospira platensis* (Class: cyanophyceae) and evaluation of their biomedical activities. *Nanomaterial*. 2021;11:95. doi:10.3390/nano11010095
70. Lashin I, Fouda A, Gobouri AA, Azab E, Mohammedsaleh ZM, Makharita RR. Antimicrobial and in vitro cytotoxic efficacy of biogenic silver nanoparticles (Ag-NPs) fabricated by callus extract of *Solanum incanum* L. *Biomolecul*. 2021;11:341. doi:10.3390/biom11030341
71. Huang L, Li D, Lin Y, Evans DG, Duan X. Influence of nano-MgO particle size on bactericidal action against *Bacillus subtilis* var. *Niger Chin Sci Bull*. 2005;50:514–519. doi:10.1007/BF02897474
72. Raliya R, Tarafdar JC. Biosynthesis and characterization of zinc, magnesium, and titanium nanoparticles: an eco-friendly approach. *Int Nano Lett*. 2014;4:1–10. doi:10.1007/s40089-014-0093-8
73. Ammulu MA, Viswanath KV, Giduturi AK, Vemuri PK, Mangamuri U, Poda S. Phytoassisted synthesis of magnesium oxide nanoparticles from *Pterocarpus marsupium* Rox. B heartwood extract and its biomedical applications. *J Genet Eng Biotechnol*. 2021;19:1–18. doi:10.1186/s43141-021-00119-0
74. Sami S. Synthesis and characterization of magnesium hydroxide nanoparticles via sol-gel. *Malays NANO Inter J*. 2022;2:36–43. doi:10.22452/mnij.vol2no2.4
75. Hamza MF, Wei Y, Mira HI, Adel H, Guibal E. Synthesis and adsorption characteristics of grafted hydrazinyl amine magnetite-chitosan for Ni (II) and Pb (II) recovery. *J Chem Eng*. 2019;362:310–324. doi:10.1016/j.cej.2018.11.225
76. Sun Y, Wang X, Ding C, et al. Direct synthesis of bacteria-derived carbonaceous nanofibers as a highly efficient material for radionuclides elimination. *ACS Sustainable Chem Eng*. 2016;4:4608–4616.
77. Jurado-López B, Vieira RS, Rabelo RB, Beppu MM, Casado J, Rodríguez-Castellón E. Formation of complexes between functionalized chitosan membranes and copper: a study by angle-resolved XPS. *Mater Chem Phys*. 2017;185:152–161. doi:10.1016/j.matchemphys.2016.10.018
78. Wei Y, Rakhatkyzy M, Salih KA, Wang K, Hamza MF, Guibal E. Controlled bi-functionalization of silica microbeads through grafting of amidoxime/methacrylic acid for Sr (II) enhanced sorption. *Chem Eng J*. 2020;402:125220. doi:10.1016/j.cej.2020.125220
79. Yang K, Zhong L, Guan R, et al. Carbon felt interlayer derived from rice paper and its synergistic encapsulation of polysulfides for lithium-sulfur batteries. *Appl Surf Sci*. 2018;441:914–922. doi:10.1016/j.apsusc.2018.02.108
80. Perera W, Dissanayake RK, Ranatunga U, et al. Curcumin-loaded zinc oxide nanoparticles for activity-enhanced antibacterial and anticancer applications. *RSC Adv*. 2020;10:30785–30795. doi:10.1039/D0RA05755J
81. Adhim AA, Abbas NR, Kadhum HH, et al. Investigating the effects of biogenic zinc oxide nanoparticles produced using *Papaver somniferum* extract on oxidative stress, cytotoxicity, and the induction of apoptosis in the THP-1 cell line. *Biol Trace Elem Res*. 2023;201:4697–4709. doi:10.1007/s12011-023-03574-7
82. Wahab R, Kaushik NK, Verma AK, et al. Fabrication and growth mechanism of ZnO nanostructures and their cytotoxic effect on human brain tumor U87, cervical cancer HeLa, and normal HEK cells. *JBIC J Biol Inorg Chem*. 2011;16:431–442. doi:10.1007/s00775-010-0740-0
83. Goorabjavari SVM, Golmohamadi F, Haririmonfared S, et al. Thermodynamic and anticancer properties of inorganic zinc oxide nanoparticles synthesized through the co-precipitation method. *J Mol Liq*. 2021;330:115602. doi:10.1016/j.molliq.2021.115602
84. Namvar F, Rahman HS, Mohamad R, et al. Cytotoxic effects of biosynthesized zinc oxide nanoparticles on murine cell lines. *J Evid Based Complementary Altern Med*. 2015;593014. doi:10.1155/2015/593014
85. Almatroudi A, Alsahli MA, Alrumaihi F, Allemailem KS, Rahmani AHJ. Ginger: a novel strategy to battle cancer through modulating cell signaling pathways: a review. *Curr Pharm Biotechnol*. 2019;20:5–16. doi:10.2174/1389201020666190119142331
86. Pei XD, He ZL, Yao HL, et al. 6-Shogaol from ginger shows anti-tumor effect in cervical carcinoma via the PI3K/Akt/mTOR pathway. *Eur J Nutr*. 2021;60:2781–2793. doi:10.1007/s00394-020-02440-9
87. Ali S, Sudha KG, Thiruvengadam M, Govindasamy R. Biocompatible synthesis of magnesium oxide nanoparticles with effective antioxidant, antibacterial, and anti-inflammatory activities using *Magnolia champaca* extract. *Biomass Convers Biorefin*. 2024;14:21431–21442. doi:10.1007/s13399-023-04252-3
88. El-Gammal RE. Antioxidative activity of nanoparticles of rosemary. *Int J ChemTech Res*. 2016;9:844–854.
89. Ratan ZA, Haidere MF, Costa JJ, Runa NJ, Hosseinzadeh H, Cho JY. Overview of inflammation. *Recent Adv Microb Diversity*. 2022;29–51. doi:10.1016/B978-0-12-822368-0.00003-7
90. Kamal M, Abdel-Raouf N, Sonbol H, et al. *In vitro* assessment of antimicrobial, anti-inflammatory, and schisto-larvicidal activity of macroalgae-based gold nanoparticles. *Front Mar Sci*. 2022;9:1075832. doi:10.3389/fmars.2022.1075832
91. Kedi PBE, Meva FE, Kotsedi L, et al. Eco-friendly synthesis, characterization, *in vitro* and *in vivo* anti-inflammatory activity of silver nanoparticle-mediated *Selaginella myosurus* aqueous extract. *Int J Nanomed*. 2018;13:8537–8548.
92. Imath M, Ragavendran C, Kamaraj C, et al. *Fioria vitifolia*-mediated silver nanoparticles: eco-friendly synthesis and biomedical potential. *J Water Process Eng*. 2024;66:106020. doi:10.1016/j.jwpe.2024.106020